The Astrophysical Journal, 630:837–863, 2005 September 10

THE CENTRAL REGION OF BARRED GALAXIES: MOLECULAR ENVIRONMENT, STARBURSTS, AND SECULAR EVOLUTION

Shardha Jogee,[1] Nick Scoville,[2] and Jeffrey D. P. Kenney[3]
Received 2004 February 13; accepted 2005 May 19

ABSTRACT

Stellar bars drive gas into the circumnuclear (CN) region of galaxies. To investigate the fate of the CN gas and star formation (SF), we study a sample of barred nonstarbursts and starbursts with high-resolution CO, optical, Hα, radio continuum, Brγ, and *HST* data, and find the following. (1) The inner kiloparsec of bars differs markedly from the outer disk. It hosts molecular gas surface densities $\Sigma_{\rm gas\text{-}m}$ of 500–3500 $M_\odot$ pc^{-2}, gas mass fractions of 10%–30%, and epicyclic frequencies of several 100–1000 km s^{-1} kpc^{-1}. Consequently, in the CN region gravitational instabilities can only grow at high gas densities and on short timescales, explaining in part why powerful starbursts reside there. (2) Across the sample, we find bar pattern speeds with upper limits of 43–115 km s^{-1} pc^{-1} and outer inner Lindblad resonance radii of >500 pc. (3) Barred starbursts and nonstarbursts have CN SF rates of 3–11 and 0.1–2 $M_\odot$ yr^{-1}, despite similar CN gas masses. The $\Sigma_{\rm gas\text{-}m}$ value in the starbursts is larger (1000–3500 $M_\odot$ pc^{-2}) and close to the Toomre critical density over a large region. (4) Molecular gas makes up 10%–30% of the CN dynamical mass and fuels large CN SF rates in the starbursts, building young, massive, high-V/σ components. Implications for secular evolution along the Hubble sequence are discussed.

Subject headings: galaxies: evolution — galaxies: ISM — galaxies: spiral — stars: formation

1. INTRODUCTION

It is widely recognized that nonaxisymmetries, such as large-scale stellar bars, facilitate the radial transfer of angular momentum in disk galaxies, thus driving their dynamical and secular evolution (e.g., Pfenniger & Norman 1990; Friedli & Benz 1995; Athanassoula 1992; Kormendy 1993; Kormendy & Kennicutt 2004; review by Jogee 2005 and references therein). Numerous studies (e.g., Knapen et al. 2000; Eskridge et al. 2002) have shown that the majority (>70%) of nearby disk galaxies host large-scale stellar bars. Using *Hubble Space Telescope* (*HST*) Advanced Camera for Surveys data, Jogee et al. (2004a, 2004b) find that strong bars remain frequent from the present day out to look-back times of 8 Gyr ($z \sim 1$), and infer that bars are long-lived features with a lifetime well above 2 Gyr. A nondeclining optical bar fraction out to $z \sim 1$ is also confirmed by Elmegreen et al. (2004). These findings suggest that bars can influence a galaxy over a significant part of its lifetime. Compelling evidence that bars efficiently drive gas from the outer disk into the inner kiloparsec comes from the larger central molecular gas concentrations observed in barred galaxies compared to unbarred galaxies (Sakamoto et al. 1999).

However, few high-resolution studies based on large samples exist of the fate of gas once it reaches the inner kiloparsec of a bar. In this study, we use high-resolution (2″; ~200 pc) CO $J = 1-0$ observations, optical, NIR, Hα, radio continuum (RC), Brγ, and archival *HST* data in order to characterize the molecular environment, the onset of starbursts, and the dynamical evolution in the circumnuclear region of barred galaxies. Our sample consists of 10 carefully selected nearby barred nonstarbursts and starbursts, including some of the most luminous starbursts within 40 Mpc. Given the time-consuming nature of interferometric 2″ CO observations, this is one of the largest samples studied at this resolution. CO observations of nearby galaxies have in the past often been limited to a few individual systems, and it is only in recent years that we have seen a systematic mapping of sizable samples (10–12) of nearby galaxies (e.g., Baker 2000; Jogee 1999). Complementary surveys such as the 7″ resolution BIMA CO (1–0) Survey of Nearby Galaxies (Regan et al. 2001; Helfer et al. 2001; Sheth et al. 2005) or the NMA-OVRO 4″ resolution CO (1–0) survey of galaxies (Sakamoto et al. 1999) are better suited for studying extended structures or the average properties within the inner kiloparsec.

The main sections of the paper are as follows. Section 2 outlines the sample selection, and § 3 the properties of stellar bars in the sample galaxies. The imaging and interferometric CO observations are covered in § 4. Section 6 highlights the extreme molecular environment that has built up in the inner kiloparsec of barred galaxies and discusses its implication. In § 7 we estimate the star formation rate (SFR) in the circumnuclear region using different tracers such as Brγ, RC, and FIR luminosities. In § 8 we compare the circumnuclear molecular gas in the barred starbursts and nonstarbursts in order to investigate why they have such different SFR/$M_{\rm H2}$ values in the inner few kiloparsecs. In § 9 we push these investigations farther by comparing the observed circumnuclear gas surface density to the critical density for the onset of gravitational instabilities. In § 10 we investigate where the molecular gas has piled up with respect to the dynamical resonances of the bar. In § 11 we discuss the results within the context of bar-driven secular evolutionary scenarios. For readers interested in specific galaxies, § 12 describes the molecular gas distribution and kinematics of individual galaxies. Section 13 summarizes our main results.

2. SAMPLE SELECTION

In this study, we wish to investigate the properties of molecular gas in the circumnuclear region (inner 1–2 kpc) of barred galaxies, the parameters that control when they form stars, and

[1] Department of Astronomy, University of Texas, 1 University Station C1400, Austin, TX 78712-0259; sj@astro.as.utexas.edu.
[2] Division of Physics, Mathematics, and Astronomy, MS 105-24, California Institute of Technology, Pasadena, CA 91125; nzs@astro.caltech.edu.
[3] Yale University, Astronomy Department, New Haven, CT 06520-8101; kenney@astro.yale.edu.

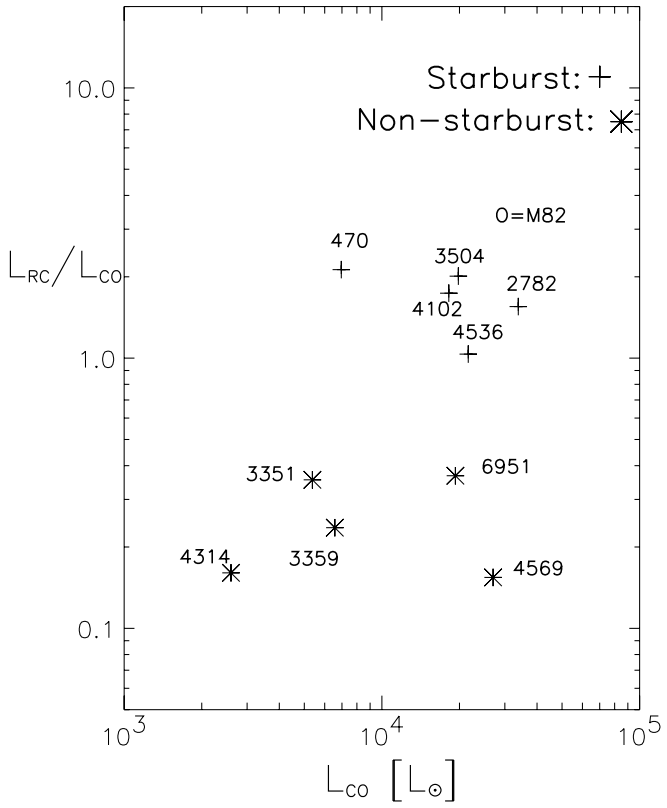

FIG. 1.—Sample of barred starbursts and nonstarbursts. L_{RC} is the RC luminosity at 1.49 GHz, and L_{CO} is the single-dish CO luminosity. Both are measured in the central 45″ diameter or inner 1–2 kpc radius. The galaxies in our sample (designated by their NGC numbers), as well as the prototypical starburst M82, are plotted. Note that for a given L_{CO}, the SFR per unit mass of molecular hydrogen as characterized by L_{RC}/L_{CO} can vary by an order of magnitude.

the reasons for the large range in SFR/M_{H2} values seen in the inner few kiloparsecs. In order to effectively address these questions, we carry out high-resolution (2″) interferometric CO observations (§ 2) of the sample galaxies. However, when selecting the sample prior to such observations, we necessarily have to use existing low-resolution (45″) single-dish CO luminosities (e.g., Young et al. 1995) as a first measure of the mass of cold molecular hydrogen (Dickman et al. 1986; Scoville & Sanders 1987). We obtain a measure of the massive SFR within the same 45″ aperture from the RC luminosity (L_{RC}) at 1.5 GHz (e.g., Condon et al. 1990). Empirical evidence such as the FIR-RC correlation (Condon et al. 1982) and the Hα-RC correlation (Kennicutt 1983), as well as simple physical models (e.g., Condon 1992), suggests that the RC luminosity at 1.5 GHz is a good tracer of the massive SFR on sufficiently large scales. The FIR-radio correlation also appears to hold locally within individual galaxies, at least on scales $\geq$1 kpc (Condon 1992).

We have selected 10 sample galaxies that satisfy the following criteria. (1) We avoided systems with very low CO luminosities, which require inordinate investments of time for interferometric CO observations. Instead, we picked galaxies that are fairly gas-rich but still span an order of magnitude in circumnuclear molecular gas content [a few $\times$ (10^8–10^9 $M_\odot$)] and a wide range in SFR per unit mass of gas. These galaxies were chosen from different parts of the L_{RC}/L_{CO} versus L_{CO} plane (Fig. 1). (2) They have moderate distances (D = 10–34 Mpc) so that the 2″ interferometric CO observations (§ 2) can accurately resolve the gas distribution and kinematics on scales of 100–300 pc. (3) They have inclinations below 70° so that we can minimize extinction problems and get a good handle on the gas kinematics. (4) They have complementary high-resolution observations such as Brγ fluxes (Puxley et al. 1988, 1990) and/or 5 GHz RC observations (Saikia et al. 1994) for tracing the SF activity at resolutions comparable to that of the 2″ interferometric CO observations. (5) We excluded major mergers with strong morphological distortions

TABLE 1
THE SAMPLE

NGC Number (1)	R.A. (B1950.0) (2)	Decl. (B1950.0) (3)	Type (4)	i (deg) (5)	D (Mpc) (6)	D_{25} (arcmin) (7)	m_B (8)	Notes (9)
Circumnuclear Starbursts								
NGC 470	01 17 10.5	03 08 53	SABb(rs)	57	30.5	3.2	12.37	D, H II
NGC 2782 (Arp 215)	09 10 54.1	40 19 18	SABa(rs)pec	30	34	3.9	12.0	D, H II
NGC 3504	11 00 28.1	28 14 35	SABab(s)	22	20.0	2.6	11.74	D, H II
NGC 4102	12 03 51.6	52 59 23	SABb(s)	52	17.0	3.1	12.13	D, L
NGC 4536	12 31 53.6	02 27 50	SABbc(rs)	66	18.0	6.3	10.60	H II, L
Circumnuclear Nonstarbursts								
NGC 3351	10 41 19.7	11 58 00	SBb(r)	46	10.1	7.5	10.28	H II
NGC 3359	10 43 21.1	63 29 11	SBc(rs)	55	19.2	7.2	10.83	H II
NGC 4314	12 20 02.1	30 10 25	SBa(rs)	21	9.7	4.2	11.28	L
NGC 4569	12 34 18.7	13 26 20	SABab(rs)	64	16.8	8.8	9.86	H II, L
NGC 6951	20 36 37.7	65 55 48	SABbc(rs)	44	18.8	3.7	11.18	Sy2

NOTES.—Cols. (2)–(3): Right ascension and declination of the optical center, from RC3. Units of right ascension are hours, minutes, and seconds, and units of declination are degrees, arcminutes, and arcseconds. Col. (4): Hubble types from RC3. Col. (5) Inclination of the galaxy. Sources are as follows: NGC 2782, Jogee et al. (1998, 1999); NGC 3351, Grosbøl (1985); NGC 3359, Martin & Roy (1995); NGC 6951, Grosbøl (1985); NGC 4314, Benedict et al. (1996); remaining galaxies, the Nearby Galaxies (NBG) Catalog (Tully 1988). Col. (6): Adopted distance. Sources are as follows: NGC 4536, Saha et al. (1996); NGC 3504, Kenney et al. (1993); NGC 2782, Jogee et al. (1998, 1999); remaining galaxies, the NBG Catalogue, which assumes a Hubble constant of 75 km s^{-1} Mpc^{-1}. Col. (7): Diameter of the isophote where the surface brightness is 25 mag arcsec^{-2} in blue light. Values are from the NBG Catalogue. Col. (8): Blue apparent magnitude corrected for reddening, from the NBG Catalogue. Col. (9): Description of the nuclear activity and optical emission line spectrum of the galaxy. D denotes a galaxy belonging to Devereux's (1989) sample of circumnuclear starbursts, H II denotes an H II region–like spectrum (Giuricin et al. 1994), L denotes a LINER (Giuricin et al. 1994), and Sy2 denotes a Seyfert 2 galaxy (Giuricin et al. 1994; Wozniak et al. 1995).

TABLE 2
SINGLE-DISH CO LUMINOSITIES AND TRACERS OF STAR FORMATION

NGC Number (1)	$S_{CO,s}$ 45″ (Jy km s^{-1}) (2)	L_{CO} 45″ ($L_\odot$) (3)	L_{RC} 45″ ($L_\odot$) (4)	$L_{10\,\mu m}$ 5″–10″ ($L_\odot$) (5)	L_{FIR} ($L_\odot$) (6)	L_{RC}/L_{CO} 45″ (7)
Circumnuclear Starbursts						
470	68	3.83	4.17	9.12	10.21	2.10
2782	266	4.50	4.72	9.02	10.42	1.60
3504	450	4.30	4.60	9.11	10.31	1.99
4102	572	4.26	4.50	9.23	10.55	1.74
4536	607	4.33	4.35	8.77	10.32	1.03
Circumnuclear Nonstarbursts						
3351	479	3.73	3.28	7.51	9.52	0.35
3359	162	3.82	3.19	...	9.90	0.23
4314	251	3.41	2.62	<7.38	8.78	0.16
4569	870	4.43	3.62	8.48	9.98	0.15
6951	496	4.28	3.85	...	9.95	0.37

NOTES.—Col. (2): Single-dish CO flux measured in the central 45″ for all galaxies except NGC 4314, where the aperture is 55″. $S_{CO,s}$ was estimated from observations with the Five College Radio Observatory (FCRAO) 14 m dish (Young et al. 1995) and NRAO 12 m single dish observations (Sage 1993). To derive flux densities $S_{CO,s}$ in units of Jy km s^{-1} from the integrated intensity I_{CO} in units of K(T_A^*) km s^{-1}, we adopted a main-beam efficiency of 42 and 35 Jy K^{-1} respectively for the FCRAO (Young et al. 1995) and NRAO (e.g., Maiolino et al. 1997) observations, and a source-beam coupling efficiency of 0.7. Col. (3): Single-dish CO luminosity (in logarithmic units of $L_\odot$) determined from $S_{CO,s}$. Col. (4): RC luminosity at 1.5 GHz in the central 45″, in logarithmic units of $L_\odot$ (Condon et al. 1990). Col. (5): Nuclear 10 μm luminosity in a central 5″–10″ aperture, in logarithmic units of $L_\odot$ (Giuricin et al. 1994). Col. (6): Far-infrared luminosity from the whole galaxy (in logarithmic units of $L_\odot$), measured in a bandpass 80 μm wide centered on a wavelength of 82.5 μm, from the *IRAS* Bright Galaxy Sample (Soifer et al. 1989). Col. (7): Ratio of the RC luminosity at 1.49 GHz to the CO luminosity. Both luminosities are measured within the same 45″ aperture, except for NGC 4314.

in the inner kiloparsec region, as the associated highly nonaxisymmetric gas distributions and large noncircular motions often preclude an accurate dynamical analysis. This is discussed further in § 3.

Table 1 gives the general properties of the sample. Table 2 shows L_{CO}, L_{RC}, and the luminosities of different SF tracers within various apertures. Figure 1 shows the sample galaxies plotted in the L_{RC}/L_{CO} versus L_{CO} plane. The term "starburst" is used in a multitude of ways in the literature: in some cases, a large SF luminosity alone is used to identify a star-forming region as a starburst, while in other cases the duration of the burst is also taken into account. In this work, the term "circumnuclear starburst" refers to a luminous and short-lived episode of SF in the inner kiloparsec region. We adopt a working definition where the circumnuclear starbursts have a ratio L_{RC}/L_{CO} above 0.5, which corresponds to a gas consumption timescale M_{H2}/SFR below 1 Gyr, under standard assumptions. The Milky Way has a an SFR/M_{H2} ratio above 10^{-9} yr^{-1} and would be a nonstarburst. The circumnuclear starbursts in our sample (NGC 470, NGC 2782, NGC 3504, NGC 4102, and NGC 4536) are marked in Figure 1 and are among the most luminous starbursts within 40 Mpc. While they are selected on the basis of RC luminosities, the circumnuclear starbursts also have a large FIR luminosity, comparable to that of the prototypical starburst M82, which is marked for reference on Figure 1. Four of the starbursts (NGC 470, NGC 2782, NGC 3504, and NGC 4102) in fact belong to Devereux's (1989) sample of the 20 brightest nearby (15 Mpc $< D <$ 40 Mpc) circumnuclear starbursts selected on the basis of a high far-infrared luminosity ($L_{FIR} > 2.9 \times 10^9\ L_\odot$) and central 10 μm luminosity ($L_{10\,\mu m} > 6 \times 10^8\ L_\odot$).

Note that in Figure 1, the SFR per unit mass of molecular gas in the central 45″ spans more than an order of magnitude for a given total mass of molecular gas. Can this range be due to the different distances of the sample galaxies causing the 45″ beam to encompass regions of different sizes? We believe this is unlikely because most of the SF activity is concentrated well inside the 45″ beam, and 80% of the galaxies have comparable distances in the range 10–20 Mpc. In fact, a similar range in the SFR per unit mass of molecular gas is obtained if the central 10 μm luminosity (Giuricin et al. 1994; Devereux 1989) is used instead of the RC to trace the SFR. It is also valid to ask whether variations in the CO-to-H_2 conversion factor χ between the galaxies might reduce the range in SFR/M_{H2} in Figure 1. We refer the reader to § 5 for a discussion on χ, but note here that the somewhat lower conversion factor in starbursts suggested by some studies (Aalto et al. 1994, 1995), would in fact increase rather than reduce the range in SFR/M_{H2} in Figure 1. Therefore, it appears that the range in SFR/M_{H2} within the sample is a truly inherent property.

3. STELLAR BARS AND TIDAL INTERACTIONS IN THE SAMPLE

It is widely held that large-scale stellar bars, whether tidally or spontaneously induced, efficiently drive gas from the outer disk into the inner kiloparsec via gravitational torques, thereby building large gas concentrations (§ 1). In fact, bars are found to be the main driver of gas inflows into the circumnuclear region even in interacting systems, namely, in a large fraction of minor mergers, most intermediate 1:3 mass ratio mergers, and the early phases of most major mergers (Jogee 2005 and references therein). The properties of the sample galaxies, which have moderate to large amounts of circumnuclear molecular gas in the range of a few $\times$ (10^8–10^9) $M_\odot$, are consistent with this picture. While we have excluded systems with strong morphological distortions (§ 2), all of the sample galaxies, except for NGC 6951, show some evidence of tidal interaction in the recent past or are in environments where they could potentially have

TABLE 3
EXTERNAL DISTURBANCES AND LARGE-SCALE STELLAR BARS

NGC Number (1)	Bar Type (2)	Evidence for External Disturbances (3)
		Circumnuclear Starbursts
470	SAB	Outer disk has asymmetric Hα emission[a] and shows evidence for warping. A recent interaction with NGC 474[b] is likely.
2782	SAB	Outer galaxy shows H I tails, optical tails, and ripples.[c,d,e] A close and intermediate mass ratio interaction with a disk galaxy[c] is likely.
3504	SAB	Belongs to a group.[f] Possibly interacting with the small galaxy NGC 3512.
4102	SAB	Belongs to a group whose brightest member is NGC 3992.[g]
4536	SAB	Is in the southern extension of the Virgo Cluster.[h] Possibly interacting with NGC 4527.
		Circumnuclear Nonstarbursts
3351	SB	Belongs to a group.[f]
3359	SB	Shows evidence[i,j] of a bar that is young and possibly tidally triggered. Has a possible small bound companion.[k]
4314	SB	Belongs to a group.[f] Outer disk is unusually gas poor. The total H I to H_2 mass ratio is unusually low ($\sim$0.02).
4569	SAB	Is located in projection within 2° of the center of the Virgo Cluster. Has anemic spiral structures[l] and a truncated H I disk.[m] Optical images[n] suggest an outer warped disk. In the inner 3.5 kpc radius, the *K*-band image[a] shows an asymmetric bar, and the molecular gas has very disturbed kinematics.[a]
6951	SAB	Isolated galaxy.

NOTES.—Col. (2): Bar type according to RC3.
[a] Jogee (1999).
[b] Schweizer & Seitzer (1988).
[c] Smith (1994).
[d] Jogee et al. (1998).
[e] Jogee et al. (1999).
[f] Tully (1988).
[g] Geller & Huchra (1983).
[h] Binggeli et al. (1985).
[i] Friedli et al. (1994).
[j] Martin & Roy (1995).
[k] Ball (1986).
[l] Van den Bergh (1976).
[m] Giovanelli & Haynes (1983).
[n] Sandage & Bedke (1994).

interacted with or accreted other galaxies. All of them host large-scale stellar bars and oval distortions, which is some cases appear to be tidally triggered.

Table 3 illustrates the evidence for recent tidal interactions. NGC 470 is interacting with the large S0 galaxy NGC 474. NGC 2782 appears to have undergone a close, recent interaction with another smaller disk galaxy, and its properties have been modeled with an intermediate mass ratio (1:4) interaction by Smith (1994). NGC 3359 has a nearby companion. NGC 3504, NGC 4314, and NGC 4102 dwell in groups, while NGC 4569 and NGC 4536 are part of the Virgo Cluster. As described below, NGC 4569 shows several indications of a recent tidal disturbance.

There is evidence of stellar bars and oval distortions in all the sample galaxies, according to our optical *R*-band and NIR images, as well as the Third Reference Catalogue of Bright Galaxies (de Vaucouleurs et al. 1991, hereafter RC3; Table 3). The top panels and bottom left panel of Figure 2 illustrate the prominent bars in NGC 3504, NGC 4314, and NGC 6951. In other cases, such as NGC 4102, NGC 4536, or NGC 2782, there is less conspicuous evidence of a large-scale bar. Both the *K*- (Fig. 2, *bottom right*) and *R*-band images of NGC 4102 reveal a weak oval distortion, with a surface brightness profile reminiscent of a lens (Jogee & Kenney 1996). This may be the remnant of a weakened or destroyed bar. In NGC 4536, despite the large inclination (66°), prominent spiral arms in the outer disk appear to branch out from an oval structure, suggesting the presence of a large-scale stellar bar. Isophotal analysis of NIR images also indicate the presence of nested nuclear stellar bars in NGC 2782 (Jogee et al. 1999; § 12) and NGC 4314 (Friedli et al. 1996; § 12).

In the nonstarbursts NGC 3359 and NGC 4569, the stellar bar may have been recently tidally triggered. After comparing simulation results (Friedli et al. 1994) with the observed properties of NGC 3359, such as the presence of H II regions along the bar and the abundance gradient profile, Martin & Roy (1995) claim that the bar in NGC 3359 is younger than a Gyr. A nearby companion (Ball 1986) may have tidally triggered this bar. In NGC 4569, the *K*-band isophotes (§ 8.1) in the inner 45″ (3.6 kpc) are significantly more elongated than those of the outer disk and suggest the presence of a stellar barlike feature that lies at a position angle (P.A.) of $\sim$15° and extends outside the boxy bulge of diameter 30″ (2.9 kpc). The bar is more elongated to the north than to the south, and the bulge isophotes also show east-west asymmetries. Furthermore, optical images (e.g., Sandage & Bedke 1994) show a warp in the outer stellar disk. A merger event or tidal interaction is likely to be responsible for the asymmetries in the stellar and CO (§ 8.1) morphologies. Ram pressure stripping, which was previously invoked to account for the H I properties (Kenney & Young 1989; Cayatte et al. 1994), primarily affects the diffuse atomic gas only.

4. OBSERVATIONS

4.1. CO $J = 1 \rightarrow 0$ *Observations*

Table 4 describes the CO observations and channel maps. For most of the sample galaxies (NGC 470, NGC 2782, NGC

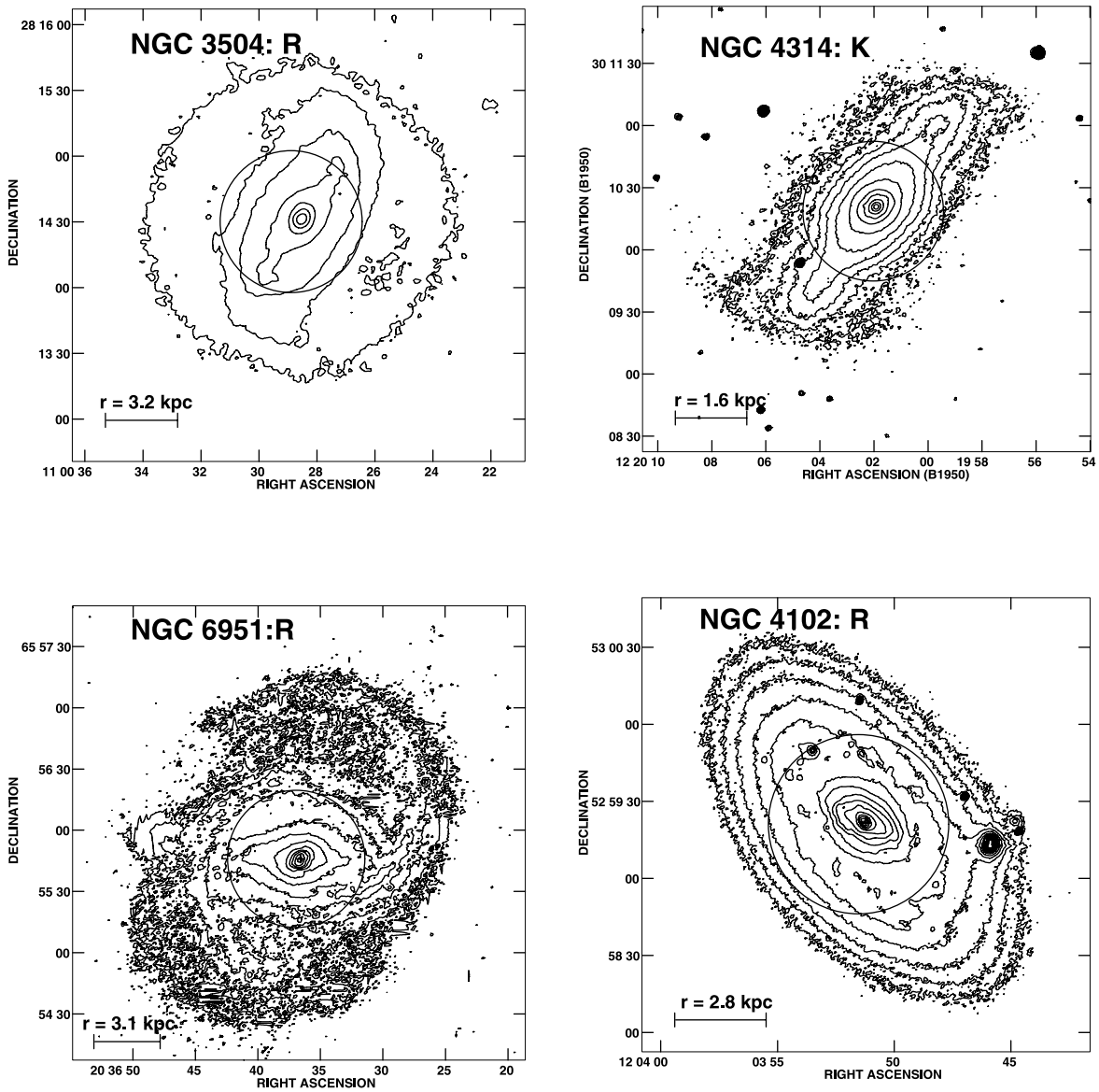

FIG. 2.—Evidence for large-scale stellar bars/oval distortions. *Top left*: *R*-band image of NGC 3504. *Top right*: *K*-band image of NGC 4314. *Bottom left*: *R*-band image of NGC 6951. *Bottom right*: *R*-band image of NGC 4102. These images illustrate the large-scale stellar bars and oval distortions in typical sample galaxies. The dotted circle shows the OVRO CO (1–0) HPBW (65″) at 115 GHz and illustrates the region where molecular gas is mapped.

TABLE 4

CO $J = 1 \rightarrow 0$ OBSERVATIONS AND CHANNEL MAPS

NGC Number (1)	Size of Synthesized Beam (2)	Weight (3)	rms Noise (mJy beam^{-1}) (4)	T_B (K) (5)
470	3″.61 × 3″.46 = 550 pc × 530 pc	U	22.0	7.4
2782	2″.14 × 1″.52 = 364 pc × 258 pc	U	13.0	28.2
	2″.62 × 1″.98 = 445 pc 337 pc	N	10.5	17.7
3504	2″.50 × 2″.40 = 250 pc × 240 pc	U	35.0	15.3
4102	2″.40 × 1″.96 = 204 pc × 167 pc	U	15.0	19.5
	3″.12 × 2″.56 = 265 pc × 218 pc	N	13.0	11.5
4536	2″.63 × 1″.88 = 235 pc × 170 pc	U	15.0	18.6
	2″.82 × 2″.37 = 255 pc × 215 pc	N	12.0	13.7
3351	2″.38 × 2″.34 = 120 pc × 118 pc	U	30.0	16.5
3359	3″.38 × 2″.91 = 324 pc × 279 pc	N	16.0	9.3
4314	2″.29 × 2″.17 = 110 pc × 105 pc	U	28.0	18.5
	3″.12 × 2″.70 = 150 pc × 130 pc	N	22.0	10.9
4569	2″.65 × 2″.01 = 225 pc × 170 pc	U	16.0	9.7
	3″.22 × 2″.95 = 275 pc × 251 pc	N	14.0	17.4
6951	2″.28 × 2″.11 = 110 pc × 102 pc	U	19.2	19.1

NOTES.—Col. (3): Weighting used for the channel maps. "U" refers to uniform and "N" to natural weighting. Col. (4): The rms noise for the channel maps. Col. (5): The equivalent brightness temperature for 1 Jy beam $^{-1}$.

3310, NGC 4102, NGC 4536, NGC 4569, and NGC 3359), 2″ observations of the CO $J = 1 \rightarrow 0$ line, whose rest frequency is 115.27 GHz, were made between 1995 and 2002 with the Owens Valley Radio Observatory (OVRO) millimeter-wave interferometer (Padin et al. 1991). The other four were observed previously by Kenney et al. (1992; NGC 3351 and NGC 6951), Kenney et al. (1993; NGC 3504), and Benedict et al. (1996; NGC 4314). As of 1996, the array consists of six 10.4 m antennae with a primary half-power beamwidth (HPBW) of 65″ at 115 GHz. The seven galaxies were observed in the low, equatorial, and high resolution configurations with projected baselines ranging from 15 to 242 m. Data were obtained simultaneously with an analog continuum correlator of bandwidth 1 GHz and a digital spectrometer setup that produced four independent modules that each have 32 channels with a velocity resolution of 10.4 km s^{-1}. For our observations, the modules were partially overlapping and covered a total bandwidth of 1200 km s^{-1} with 116 frequency channels. We corrected for temporal phase variations by interspersing integrations on the galaxy with observations of a phase calibrator (typically a quasar) every 20–25 minutes. Passbands were calibrated on the bright quasars 3C 273, 3C 84, and 3C 345. The absolute flux scale, determined from observations of Uranus, Neptune, and 3C 273, is accurate to 20%. The passband and flux calibration of the data were carried out using the Owens Valley millimeter array software (Scoville et al. 1993). We used the NRAO AIPS software to Fourier transform the calibrated *u-v* data and deconvolve the channel maps with the CLEAN algorithm as implemented in the AIPS tasks MX and IMAGR. Channel maps with both uniform and natural weighting were made for the galaxies. The naturally weighted maps capture more of the low signal-to-noise emission, but have lower spatial resolution.

4.2. *Optical Observations*

We observed the 10 sample galaxies using the Wisconsin-Indiana-Yale-NOAO (WIYN) 3.5 m telescope at Kitt Peak National Observatory (KPNO), and the 0.9 m telescope at KPNO. On the WIYN telescope we used a 2048×2048 S2KB CCD with a plate scale of 0.″2 pixel^{-1} and a field of view of $6.'8 \times 6.'8$. On the 0.9 m, the 2048×2048 T2KA CCD had a plate scale of 0.″68 pixel^{-1} and field of view of $23.'2 \times 23.'2$. The galaxies were imaged with broadband Harris *BVRI* filters, narrowband filters centered on the appropriately redshifted Hα+[N II] $\lambda\lambda$6563, 6583 emission lines, and narrow off-line filters centered on a wavelength ~80 Å redward of the Hα+[N II] line. The latter images are used to subtract stellar continuum from the Hα+[N II] image, and the continuum bandpass in this region is sufficiently close to the Hα+[N II] emission line that spectral color correction terms are generally negligible (Taylor et al. 1994). Standard fields of Landolt stars (e.g., PG 0918+029, PG 1047+003, PG 1323−086, Wolf 629, SA 110-502) were observed throughout the night over a range of air masses for extinction correction. For some galaxies, where we had photometric conditions, exposures of the galaxy and of spectrophotometric standards at similar air masses were taken for flux calibrating the Hα+[N II] observations. The IRAF package was used for data reduction. After bias-subtraction and flat-fielding, the images in each filter were registered using unsaturated field stars, combined, and cleaned free of cosmic rays. After sky subtraction, the off-line narrowband image was subtracted from the online image to obtain continuum-free Hα+[N II] line images. Where available, observations of spectrophotometric standards were used to flux calibrate the line.

5. CIRCUMNUCLEAR MOLECULAR GAS CONTENT

The mass of molecular hydrogen (M_{H2}) is estimated from the total flux using the relation (e.g., Scoville et al. 1987; Kenney & Young 1989)

$$\frac{M_{H2}}{M_\odot} = 1.1 \times 10^4 \left(\frac{\chi}{2.8 \times 10^{20}}\right) D^2 \int S_{CO} dV, \qquad (1)$$

where D is the distance in Mpc, $\int S_{CO} dV$ is the integrated CO line flux in Jy km s^{-1}, and χ is the CO-to-H_2 conversion factor, defined as the ratio of the beam-averaged column density of hydrogen to the integrated CO brightness temperature $[N(H_2)/I_{CO}]$.

The CO-to-H_2 conversion factor χ depends on many factors, including the metallicity of the gas, the dust column density, the ambient radiation field, the physical conditions in the gas, and the optical thickness of the line. All the sample targets are massive spirals and are likely to have solar or supersolar metallicities (Vila-Costas & Edmunds 1992). In this regime, the CO line is optically thick and there is only a weak dependence of χ on metallicity (e.g., Elmegreen 1989), so that our use of a single χ-value across the sample is justified.

Values of χ for molecular clouds in the Milky Way range from 1.8 to 4.5×10^{20} (K km s^{-1})$^{-1}$, based on different methods such as comparisons of the integrated ^{13}CO intensities with the visual extinction (e.g., Dickman 1975), observations of γ-ray fluxes (e.g., Bloemen et al. 1986; Strong et al. 1988), and virial equilibrium considerations (e.g., Dickman et al. 1986; Scoville et al. 1987; Solomon et al. 1987). It is arguable whether a Milky Way conversion factor applies to the actively star-forming circumnuclear regions of galaxies, where the temperatures and densities are much higher. For clouds in virial equilibrium, χ depends on $\rho^{0.5}/T_B$ (e.g., Scoville & Sanders 1987), where T_B is the CO brightness temperature averaged over the cloud and ρ is the density. One might argue, therefore, that the effects of elevated temperatures and densities will partially offset each other. On the other hand, the gas may not be in virial equilibrium, and multiple-line studies combined with radiative transfer modeling (e.g., Wall & Jaffe 1990; Helfer & Blitz 1993; Aalto et al. 1994, 1995)

TABLE 5
CIRCUMNUCLEAR MOLECULAR PROPERTIES

NGC Number (1)	$S_{CO,I}$ (Jy km s^{-1}) (2)	M_{H2} ($M_\odot$) (3)	V_{sys} (km s^{-1}) (4)	f_{SD} (%) (5)
Circumnuclear Starburst				
470	53	5.0E8	2350	80
2782	184	2.3E9	2555	65
3504	280	1.2E9	1535	71
4102	450	1.4E9	835	80
4536	355	1.2E9	1800	60
Circumnuclear Nonstarbursts				
3351	241	2.7E8	780	60
3359	20	8.0E7	...	12
4314	248	2.6E8	983	92
4569	550	1.7E9	−235	65
6951	299	1.2E9	1431	60

NOTES.—Col. (2): Flux detected by the OVRO interferometric observations. Col. (3): Mass of molecular hydrogen corresponding to $S_{CO,I}$, if one assumes a standard Galactic CO-to-H_2 conversion factor. Col. (4): Systemic velocity estimated from the moment 1 map. Col. (5): Fraction of the single-dish flux detected by the interferometric observations. See text for a discussion of the low f_{SD} for NGC 3359.

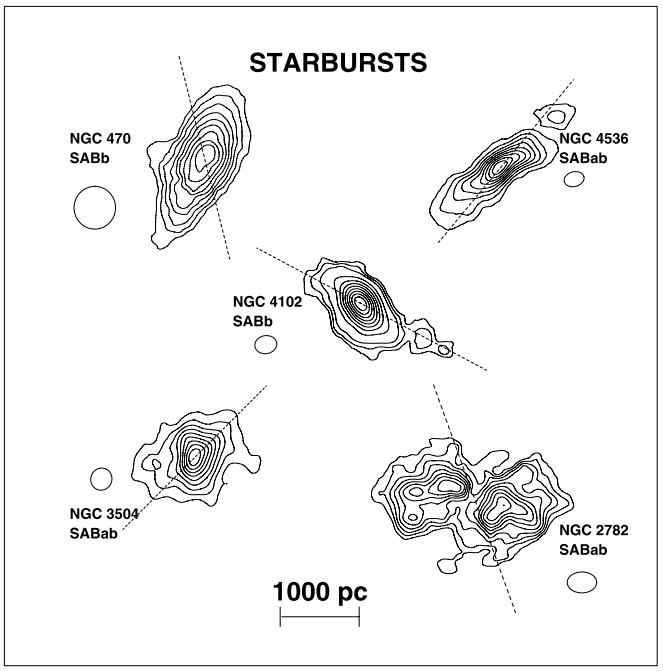

FIG. 3*a*

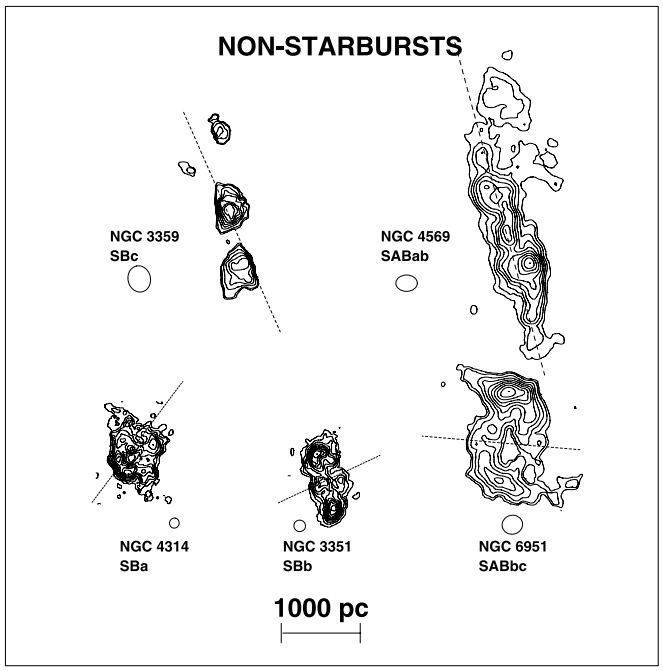

FIG. 3*b*

FIG. 3.—Circumnuclear molecular gas morphology. The CO total intensity (moment 0) maps of barred starbursts and nonstarbursts are shown. The size of the synthesized beam is shown next to each map. The dotted line shows the P.A. of the large-scale stellar bar/oval. The contour levels plotted are specified in Table 10. There is a wide variety of circumnuclear CO morphologies, including relatively axisymmetric annuli or disks (starbursts NGC 4102, NGC 3504, and NGC 4536, and nonstarburst NGC 4314), elongated double-peaked and spiral morphologies (starburst NGC 2782 and nonstarbursts NGC 3351 and NGC 6951), and extended distributions elongated along the bar (nonstarburst NGC 4569). The relationship between the gas distribution and the resonances of the bar is discussed in § 10 and Fig. 9.

have suggested that χ is lower by a factor of $\sim$3 in the centers of some starburst galaxies, as compared to the Milky Way. However, given the absence of multiple-line studies or determinations of χ in our sample galaxies, we adopt in this paper the value of 2.8×10^{20} (K km s^{-1})$^{-1}$ that was derived for the inner Galaxy (Bloemen et al. 1986), while bearing in mind the possible uncertainties.

Table 5 shows the CO flux and the mass of molecular hydrogen detected by the interferometric observations. In most galaxies, we capture a large fraction (60%–90%) of the CO flux detected by single-dish observations. We find massive gas concentrations—3×10^8 to 2×10^9 $M_\odot$ of molecular hydrogen—in the inner 2 kpc radius of the sample galaxies. In particular, many galaxies with different RC luminosities within the central 45″ (e.g., NGC 6951 and NGC 4569, as compared to NGC 2782, NGC 3504, and NGC 4102) can have quite comparable circumnuclear molecular hydrogen content [$\sim(1\text{–}2) \times 10^9$ $M_\odot$].

Figure 3 shows the CO total intensity (moment 0) maps, the size of the synthesized beam, and the position of the large-scale stellar bar for the sample galaxies. There is a wide variety of CO morphologies ranging from relatively axisymmetric annuli or disks (NGC 4102, NGC 3504, NGC 4536, NGC 470, and NGC 4314) to elongated double-peaked and spiral morphologies (starburst NGC 2782 and nonstarbursts NGC 3351 and NGC 6951). We refer the reader to § 8 for a comparison of the molecular gas properties in the starbursts and nonstarbursts, and to § 12 for a description of the individual galaxies.

6. THE EXTREME MOLECULAR ENVIRONMENT IN THE INNER KILOPARSEC OF BARRED SPIRALS AND ITS IMPLICATIONS

Table 6 illustrates how the molecular environment that has developed in the circumnuclear region of the barred spirals differs markedly from that present in the outer disk of galaxies. Here we outline the implications for the inner kiloparsec.

1. *Gas densities and mass fraction*.—We compute the molecular gas surface densities ($\Sigma_{\text{gas-m}}$) by deprojecting the moment 0 map and computing the azimuthally averaged surface density of molecular hydrogen (Σ_{H2}) as a function of radius in the galactic plane, assuming a standard CO-to-H_2 conversion factor. We add in the contribution of He using $\Sigma_{\text{gas-m}} = A_Z \times \Sigma_{\text{H2}}$, where $A_Z = 1.36$ for an assumed solar metallicity ($Z = 0.02$, $X = 0.72$, $Y = 0.26$). The peak gas surface density $\Sigma_{\text{gas-m}}$ in the inner kiloparsec of these galaxies ranges from 500 to 3500 $M_\odot$ pc^{-2}.

To estimate what fraction of the dynamical mass is in molecular form, we first calculate the total dynamical mass M_{dyn} interior to radius R from the circular speed V_c:

$$M_{\text{dyn}}(R) = \frac{V_c^2(R) R \beta}{G}, \qquad (2)$$

where G is the gravitational constant and β depends on the shape of the mass distribution; $\beta = 1$ for a spherically symmetric mass distribution and is slightly lower for flattened configurations. For an exponential disk, we can overestimate the true dynamical mass by at most 1.3 if we assume $\beta = 1$ (Binney & Tremaine 1987). We estimate V_c and the CO rotation curve in the central 1–2 kpc radius from the CO position-velocity (p-v) plots. We can more effectively identify different kinematic components (e.g., circular motions, azimuthal streaming motions, radial inflow motions, and vertical outflow motions) in gas of different intensities from p-v plots along the kinematic major and minor axes than from moment 1 maps, which reflect only the intensity-weighted average values. In particular, we estimate V_c by taking the CO velocity at which the intensity levels peak at each radius along the kinematic major axis. The values

TABLE 6

MOLECULAR ENVIRONMENTS IN THE CIRCUMNUCLEAR REGION VERSUS THE OUTER DISK

Quantities[a]	Outer Disk of Normal Sa–Sc Spirals	Inner 500 pc Radius of Sample Starbursts and Nonstarbursts	Inner 500 pc Radius of ULIRG Arp 220
$M_{\rm gas\text{-}m}$ ($M_\odot$)	$\leq$a few $\times$ 10^9 [b]	a few $\times$ (10^8–10^9)[c]	3×10^9 [d]
$M_{\rm gas}/M_{\rm dyn}$ (%)	<5[e]	10–30[c]	40–80[d]
SFR ($M_\odot$ yr^{-1})	...	0.1–11[c]	>100[f]
$\Sigma_{\rm gas\text{-}m}$ ($M_\odot$ pc^{-2})	1–100[g]	500–3500[c]	4×10^4 [d]
σ (km s^{-1})	6–10[h]	10–40[i]	90[g]
κ (km s^{-1} kpc^{-1})	<100[j]	800–3000[c]	>1000[g]
$\Sigma_{\rm crit}$ ($M_\odot$ pc^{-2})	<10[k]	500–1500[l]	2200[m]
$t_{\rm GI}$ (Myr)	>10[k]	0.5–1.5[l]	0.5[m]
$\lambda_{\rm J}$ (pc)	a few $\times$ (100–1000)[k]	100–300[l]	90[m]
$M_{\rm J}$ ($M_\odot$)	a few $\times$ (10^7–10^6)[k]	a few $\times$ (10^7–10^8)[l]	8×10^8 [m]

[a] Typical values are quoted for the quantities. Individual cases may vary. Quantities are as follows: $M_{\rm gas\text{-}m}$, the molecular gas content including hydrogen and helium (a standard CO-to-H_2 conversion factor and a solar metallicity are assumed); $M_{\rm gas\text{-}m}/M_{\rm dyn}$, the ratio of molecular gas mass to dynamical mass; $\Sigma_{\rm gas\text{-}m}$, the molecular gas surface density; $\Sigma_{\rm SFR}$, the SFR per unit area; σ, the gas velocity dispersion; κ, the epicyclic frequency; $\Sigma_{\rm crit}$, the critical density for the onset of gravitational instabilities as defined in § 9, with $\alpha = 0.7$; $t_{\rm GI} = Q/\kappa$, the growth timescale of the most unstable wavelength associated with gravitational instabilities, assuming $Q \sim 1$; $\lambda_{\rm J}$, the Jeans length; $M_{\rm J}$, the Jeans mass.

[b] Young & Scoville (1991).

[c] This work.

[d] Sakamoto et al. (1999), for a self-gravitating gas disk. Quoted mass is the sum for Arp 220 W and E.

[e] Binney & Tremaine (1987).

[f] Scoville et al. (1997).

[g] Devarheng et al. (1994).

[h] Dickey et al. (1990).

[i] The upper limit for the velocity dispersion is quoted after correcting for beam smearing.

[j] Larson (1988).

[k] For the outer disk, $\Sigma_{\rm crit}$, $t_{\rm GI}$, $\lambda_{\rm J}$, and $M_{\rm J}$ are computed for $\kappa < 100$ km s^{-1} kpc^{-1}, $\sigma \sim 6$ km s^{-1}, and $\Sigma_{\rm gas\text{-}m} = 10$—$100$ $M_\odot$ pc^{-2}.

[l] $\Sigma_{\rm crit}$, $t_{\rm GI}$, $\lambda_{\rm J}$, and $M_{\rm J}$ are computed at $r = 250$ pc in the circumnuclear starbursts and nonstarbursts NGC 4102, NGC 4536, NGC 3504, NGC 3351, and NGC 4314.

[m] $\Sigma_{\rm crit}$, $t_{\rm GI}$, $\lambda_{\rm J}$, and $M_{\rm J}$ are computed for Arp 220 W assuming $\kappa \sim 2000$ km s^{-1} kpc^{-1}, $\sigma \sim 90$ km s^{-1}, and $\Sigma_{\rm gas\text{-}m} \sim 4 \times 10^4$ $M_\odot$ pc^{-2}.

of V_c estimated in this manner show good agreement with the rotation curve derived from Hα emission spectra (Jogee 1999) in cases where both data are available (e.g., NGC 4102, NGC 4536, NGC 3351, NGC 4569, NGC 6951). In regions where the gas shows evidence of noncircular motions in the p-v plots, estimates of V_c will be somewhat uncertain. We therefore derive V_c only for galaxies where the kinematics are relatively ordered and dominated by circular motions (§ 8).

In summary, we find that the inner kiloparsec of the 10 barred spirals in our sample hosts peak molecular gas surface densities of 500–3500 $M_\odot$ pc^{-2} and molecular gas mass fractions of 10%–30%. These densities are at least an order of magnitude higher than the typical average atomic and molecular gas surface densities (1–100 $M_\odot$ pc^{-2}) in the outer disk of normal spirals (Deharveng et al. 1994; Kennicutt 1998b) or the gas surface density (200 $M_\odot$ pc^{-2}) of a typical giant molecular cloud in the outer disk of the Milky Way (Scoville & Sanders 1987). Such large molecular gas surface densities and mass fractions in the inner kiloparsec can enhance the self-gravity and clumpiness of the gas and produce stronger gravitational coupling between the gas and the stars (e.g., Shlosman et al. 1989; Jog & Solomon 1984). The resulting two-fluid disk will be more unstable to gravitational instabilities than a purely stellar one-fluid disk (Jog & Solomon 1984; Elmegreen 1995).

Furthermore, as the gas becomes more clumpy, dynamical friction might become an increasingly important transport mechanism at low radii. For instance, in the case of a gas clump that has a mass M and a speed v at radius r, the timescale $t_{\rm df}$ on which dynamical friction operates is $\propto(r^2 v/M \ln \Lambda)$, where $\ln \Lambda$ is the Coulomb logarithm (Binney & Tremaine 1987). For $M = 10^8$ $M_\odot$, $v \sim 300$ km s^{-1}, and $r = 200$ pc, $t_{\rm df}$ is as short as $\sim 3 \times 10^6$ yr.

2. *Onset and growth of gravitational instabilities*.—For a thin differentially rotating gas disk, support against gravitational instabilities is provided by pressure forces on small scales and by Coriolis forces from rotation on large scales. The Coriolis forces depend on the epicyclic frequency of oscillations κ, which is a function of the circular speed V_c:

$$\kappa = \sqrt{\frac{2V_c}{R}\left(\frac{V_c}{R} + \frac{dV_c}{dR}\right)}. \quad (3)$$

We estimate κ from the CO and Hα rotation curves, bearing in mind that uncertainties exist in regions where there are noncircular motions. However, even uncertainties of a factor of a few do not change the basic expectations of very high epicyclic frequencies κ of a few 100 to several 1000 km s^{-1} kpc^{-1} in the inner 500 pc. These very high epicyclic frequencies coupled with the moderately large gas velocity dispersions (10–40 km s^{-1}) cause the critical density $\Sigma_{\rm crit}$ for the onset of gravitational instabilities to shoot up to several 100–1000 $M_\odot$ pc^{-2}. Although hard to trigger, once triggered, these instabilities have a short growth timescale $t_{\rm GI}$ of a few Myr for the most unstable wavelength:

$$t_{\rm GI} = \frac{\sigma}{\pi G \Sigma_{\rm gas}}. \quad (4)$$

In other words, the molecular environment and dynamical parameters of the inner kiloparsec naturally force gravitational instabilities to set in and to grow in a "burst" mode defined by high density and short timescales. This may explain, at least in part, why the most intense starbursts tend to be found in the inner kiloparsec of galaxies.

It is also important to note that the growth timescale $t_{\rm GI}$ of a few Myr in the inner kiloparsec is comparable to the lifetime of

TABLE 7
STAR FORMATION RATES FROM FAR-INFRARED, RADIO CONTINUUM, AND Brγ DATA

	BASED ON GLOBAL L_{FIR}		BASED ON RC				BASED ON Brγ		
NGC NUMBER (1)	L_{FIR} ($L_\odot$) (2)	SFR_{FIR} ($M_\odot$ yr^{-1}) (3)	ν (GHz) (4)	S_ν (mJy) (5)	R_{RC} (pc) (6)	SFR_{RC-N} ($M_\odot$ yr^{-1}) (7)	$R_{Br\gamma}$ (pc) (8)	N_{Ly} (s^{-1}) (9)	$SFR_{Br\gamma}$ ($M_\odot$ yr^{-1}) (10)
Circumnuclear Starbursts									
470	10.21	6.3	1.5	26.6[a]	1680	2.8	...	...	...
2782	10.42	10.2	1.5	107[a]	2210	13.8	1650	5.0E53[b]	5.6
	...	...	4.9	40[c]	1700	11.6	...	...	...
3504	10.31	8.0	1.5	230[a]	800	10.2	945	1.5E53[b]	2.8
4102	10.55	13.8	1.5	227[a]	1105	7.3	945	9.2E52[b]	1.1
4536	10.32	8.1	1.5	149[a]	1800	5.4	840	4.0E53[b]	4.8
	...	...	4.9	61[d]	900	4.9	...	...	...
Circumnuclear Nonstarbursts									
3351	9.52	1.3	1.5	28[e]	1000	0.3	490	6.0E52[b]	0.5
3359	9.90	3.1	1.5	50[a]	20160	2.1	...	...	...
4314	8.78	0.2	1.5	12.5[f]	3640	0.1	...	...	...
4569	9.98	3.7	1.5	83[f]	8420	2.5	...	...	...
6951	9.95	3.5	4.9	14[c]	750	1.2	...	...	...

NOTES.—Col. (2): Global FIR luminosity in logarithmic units of $L_\odot$. Col. (3): Global SFR for the entire galaxy. Col. (4): Frequency of the RC observations. Col. (5): RC flux density. Col. (6): Radius within which more than 90% of the RC emission is concentrated. Col. (7): SFR within R_{RC}, estimated from the nonthermal component of the radio continuum flux density. Col. (8): Aperture radius for the Brγ observations. Col. (9): Number of Lyman continuum photons per second from Puxley et al. (1990). Col. (10): SFR within $R_{Br\gamma}$.

[a] Condon et al. (1990).
[b] Puxley et al. (1990).
[c] Saikia et al. (1994).
[d] Vila et al. (1990).
[e] Condon et al. (1995).
[f] Condon (1987).

an OB star. As a result, the fraction of molecular gas mass converted into stars before cloud complexes are disrupted by massive stars can be higher in the circumnuclear region than in the outer disk. The high-pressure, high-turbulence ISM may also favor more massive clusters, as suggested by some authors (e.g., Elmegreen et al. 1993). It is relevant that 80% of the sample galaxies show super star clusters.

3. *ULIRGs as scaled-up local starbursts?*—In the circumnuclear region of the ULIRG Arp 220 (Scoville et al. 1997), the conditions observed seem to be even more extreme than those in the inner kiloparsec of the local barred starbursts: a gas surface density $\sim 10^4\ M_\odot\ pc^{-2}$, a velocity dispersion $\sigma \sim 90$ km s^{-1}, and an epicyclic frequency $\kappa \sim$ several 1000 km s^{-1} kpc^{-1} (Table 6). Observations of these quantities at comparable resolutions do not exist for other ULIRGs, but if Arp 220 is a prototypical ULIRG, then Table 6 suggests that the circumnuclear molecular environment of ULIRGs is a scaled-up version of that developed by the local weakly interacting starbursts in our sample. This scaled-up molecular environment may be the result of the stronger external triggers acting on ULIRGs, which are generally strongly interacting systems, often involving mergers of comparably massive spirals. Such interactions can pile gas to very high densities in the inner kiloparsec and produce larger turbulent line widths, thereby boosting the critical density Σ_{crit} at which gravitational instabilities set in and ensuring the conditions for a superstarburst.

7. THE CIRCUMNUCLEAR STAR FORMATION RATE

When using the 45″ single-dish CO map as a measure of the circumnuclear gas content (e.g., in § 2), it was appropriate to use the RC luminosity within a similar 45″ aperture as a measure of the circumnuclear SFR. The 45″ aperture corresponds to an aperture with a 2 kpc radius at the mean sample distance of 20 Mpc. However, now that we have obtained high-resolution (2″) interferometric CO maps, we need to resolve the SF activity and estimate the SFR within the radius (R_{CO}), which encompasses most of the detected CO emission. We denote this as SFR_{CO}. We can then verify whether the large range in SFR/M_{H2} seen within the sample when using 45″ averaged data persists even at higher resolution. The radius R_{CO} is estimated by determining where the azimuthally averaged gas surface density falls below a few percent of its peak value, and ranges from 500 to 1680 pc (Table 8).

We estimate SFR_{CO} within R_{CO} by considering an ensemble of SFRs derived from different tracers that each may offer a different advantage in terms of resolution, apertures, and extinction. For instance, a well-established physical framework exists linking Hα recombination lines to the UV continuum photons from massive young stars (e.g., Kennicutt 1998a), but Hα fluxes can be strongly affected by extinction in the dusty circumnuclear region, where gas densities reach several 100 to 1000 $M_\odot\ pc^{-2}$. Conversely, tracers such as the far-infrared or RC luminosity are less affected by extinction but have lower spatial resolution such that they may not always resolve the SF within R_{CO}.

Following Condon (1992) and Kennicutt (1998a), we estimate the SFRs from (1) the global FIR luminosity, (2) the Brγ luminosity, and (3) the nonthermal and thermal components of the RC emission, which we denote respectively as SFR_{FIR}, $SFR_{Br\gamma}$, SFR_{RC-N}, and SFR_{RC-T}. Table 7 summarizes the values and apertures for each tracer.

1. *SFR based on the global FIR luminosity (SFR_{FIR}).*—The global FIR luminosity traces the massive SFR over the entire

galaxy, under the assumption that most of the FIR emission between 40 and 120 μm emanates from warm dust heated by massive stars. SFR_{FIR} was computed from

$$\frac{\mathrm{SFR}}{M_\odot\ \mathrm{yr}^{-1}} = 4.3 \times \mathrm{SFR}(M \geq 5\ M_\odot) = \gamma \times \left(\frac{L_{\mathrm{FIR}}}{10^{10}\ L_\odot}\right), \quad (5)$$

where $\mathrm{SFR}(M \geq 5\ M_\odot)$ is the rate of formation of stars with mass $M \geq 5\ M_\odot$. An extended Miller-Scalo IMF (Kennicutt 1983) with an upper mass cutoff M_U of 100 $M_\odot$ is assumed. We adopt $\gamma = 3.9$ (Condon 1992). As shown in Table 7, the global SFR ranges from 6 to 14 $M_\odot\ \mathrm{yr}^{-1}$ for the starbursts and from 0.2 to 4 $M_\odot\ \mathrm{yr}^{-1}$ for the nonstarbursts. These values apply to the entire galaxy and therefore serve as an upper limit to the SFR in the circumnuclear region.

2. *SFR based on the nonthermal and thermal component of the RC emission ($SFR_{RC\text{-}N}$, $SFR_{RC\text{-}T}$).*—The thermal free-free emission from the photoionized H II regions and the nonthermal RC emission produced by relativistic electrons that are accelerated by supernova remnants are both related to the massive SFR. The RC flux density at 1.5 and 4.9 GHz is dominated by nonthermal emission. We estimate the nonthermal fraction to be 0.88 at 1.5 GHz and 0.77 at 4.9 GHz following the approximation by Condon & Yin (1990):

$$\frac{S}{S_T} = 1 + 10 \times \left(\frac{\nu}{\mathrm{GHz}}\right)^{0.1-\alpha}, \quad (6)$$

where the nonthermal index α is $\sim$0.8. From the nonthermal component of the RC luminosity density ($L_{N\nu}$), we estimate the star formation rate $\mathrm{SFR_{RC\text{-}N}}$ within the radius R_{RC} using

$$\frac{\mathrm{SFR_{RC\text{-}N}}}{M_\odot\ \mathrm{yr}^{-1}} = 4.3 \times 0.019 \times \left(\frac{\nu}{\mathrm{GHz}}\right)^{\alpha} \left(\frac{L_{N\nu}}{10^{20}\ \mathrm{W\ Hz}^{-1}}\right). \quad (7)$$

This equation assumes the Galactic relationship between the supernova rate and the RC luminosity density (Condon 1992). As shown in Table 7, $\mathrm{SFR_{RC\text{-}N}}$ applies to the region of radius R_{RC} that covers the inner 1-2 kpc, except for NGC 3359 and NGC 4314, where larger apertures apply. $\mathrm{SFR_{RC\text{-}N}}$ ranges from 3 to 14 $M_\odot\ \mathrm{yr}^{-1}$ for the starbursts and from 0.1 to 2 $M_\odot\ \mathrm{yr}^{-1}$ for the nonstarbursts. When estimating SFRs in NGC 6951, we excluded the luminosity contribution from the inner 100 pc radius to avoid contamination from the Seyfert nucleus that is known to exist from optical line ratios (Muñoz-Tuñon et al. 1989).

We estimate $\mathrm{SFR_{RC\text{-}T}}$ from the thermal component of the RC emission ($L_{T\nu}$) using

$$\frac{\mathrm{SFR_{RC\text{-}T}}}{M_\odot\ \mathrm{yr}^{-1}} = 4.3 \times 0.176 \times \left(\frac{L_{T\nu}}{10^{20}\ \mathrm{W\ Hz}^{-1}}\right) \times \left(\frac{T_e}{10^4\ \mathrm{K}}\right)^{-0.45} \left(\frac{\nu}{\mathrm{GHz}}\right)^{0.1}. \quad (8)$$

$\mathrm{SFR_{RC\text{-}T}}$ is slightly lower than $\mathrm{SFR_{RC\text{-}N}}$, but the difference is only at the 5% level. It is encouraging that the same trend is seen in estimates based on RC ($\mathrm{SFR_{RC\text{-}N}}$) and FIR ($\mathrm{SFR_{FIR}}$) light: the starbursts have larger SFRs (3–14 $M_\odot\ \mathrm{yr}^{-1}$) than the nonstarbursts (0.1–2 $M_\odot\ \mathrm{yr}^{-1}$). Figure 4 shows $\mathrm{SFR_{RC\text{-}N}}$ plotted against $\mathrm{SFR_{FIR}}$. $\mathrm{SFR_{RC\text{-}N}}$ is comparable to $\mathrm{SFR_{FIR}}$ in all galaxies except NGC 2782 and NGC 3504, where $\mathrm{SFR_{RC\text{-}N}}$ is 10%–30% higher. This could be caused by a variety of reasons. The dust temperature and emissivities could be different from those assumed such that $\mathrm{SFR_{FIR}}$ underestimates the true

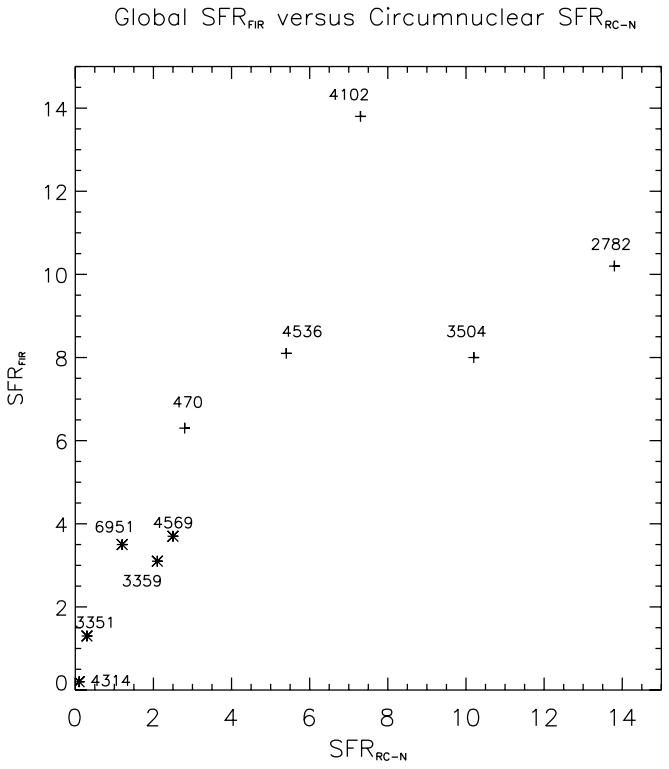

FIG. 4.—Comparison of the SFRs estimated from different tracers. $\mathrm{SFR_{RC\text{-}N}}$, the SFR estimated from the nonthermal RC in 45″, is plotted against the SFR estimated from the total FIR luminosity ($\mathrm{SFR_{FIR}}$). $\mathrm{SFR_{RC\text{-}N}}$ is less than $\mathrm{SFR_{FIR}}$, as expected, except in NGC 2782 and NGC 3504, where $\mathrm{SFR_{RC\text{-}N}}$ is 10%–30% higher.

global SFR. Another possibility is that part of the nonthermal RC emission is coming from starburst-driven outflows, where the empirical Galactic relationship between the supernova rate and the RC luminosity density might not hold. In fact, in NGC 2782, the high (1″) resolution RC map (Saikia et al. 1994) shows that a large fraction of the RC emission emanates from double outflow shells that extend 850 pc away from the central starburst (Jogee et al. 1998). Furthermore, while there is no evidence from optical line ratios for an active nucleus in these two galaxies, one cannot rule out the possibility that part of the nonthermal RC emission may be due to a hidden active nucleus.

3. *SFR based on Brγ fluxes ($SFR_{Br\gamma}$).*—The Brγ recombination line at 2.16 μm traces Lyman continuum photons from massive stars. Published Brγ fluxes (e.g., Puxley et al. 1990) are only available for four starbursts, NGC 2782, NGC 3504, NGC 4102, and NGC 4536, and for the nonstarburst NGC 3351. As shown in Table 7, the radius $R_{\mathrm{Br}\gamma}$ of the region over which Brγ observations were made varies between 500 and 1600 pc depending on the galaxy. $\mathrm{SFR_{Br\gamma}}$ is 1–6 $M_\odot\ \mathrm{yr}^{-1}$ for the starbursts and 0.5 $M_\odot\ \mathrm{yr}^{-1}$ for the nonstarburst NGC 3351, as computed from

$$\frac{\mathrm{SFR}}{M_\odot\ \mathrm{yr}^{-1}} = 11.97 \times 10^{-54} \left(\frac{N_{\mathrm{Ly}}}{\mathrm{s}^{-1}}\right). \quad (9)$$

$\mathrm{SFR_{RC\text{-}N}}$ is larger by a factor of 2–5 compared to $\mathrm{SFR_{Br\gamma}}$ in NGC 2782, NGC 3504, NGC 4102, and NGC 4536, where both SFRs are measured over comparable radii. It is likely that $\mathrm{SFR_{Br\gamma}}$ underestimates the true SFR as the Brγ data and ionization rate (N_{Ly}) quoted by Puxley et al. (1990) have not been corrected for

TABLE 8
ADOPTED CIRCUMNUCLEAR STAR FORMATION RATES OVER RADIUS OF CO EMISSION

NGC Number (1)	R_{CO} (pc) (2)	M_{H2} ($M_\odot$) (3)	SFR_{CO} ($M_\odot$ yr^{-1}) (4)	SFR_{CO}/M_{H2} (yr^{-1}) (5)	t_{SFR} (10^8 yr) (6)
Circumnuclear Starburst					
470	1100	5.0E8	3	6E−9	2
2782	1530	1.8E9	11	6E−9	2
3504	1300	1.2E9	10	8E−9	1
4102	1275	1.4E9	7	5E−9	2
4536	1300	1.2E9	5	4E−9	2
Circumnuclear Nonstarbursts					
3351	600	5.3E8	0.5	9E−10	11
4314	590	2.3E8	<0.1	<4E−10	>25
4569	1680	1.6E9	<1.2	>7E−10	>14

NOTES.—Col. (2): Radius of CO emission. Col. (3): Mass of molecular hydrogen within a radius R_{CO}. Col. (4): SFR within R_{CO}. Col. (5): SFR per unit mass of molecular hydrogen. Col. (6): Average gas consumption timescale by SF given by M_{H2}/SFR_1.

extinction at 2.2 μm. Dust within an internally dusty H II region can absorb Lyman continuum photons before they ionize any H atom, and dust along the line of sight can absorb part of the Brγ recombination photons.

Table 7 summarizes the SFR estimated (SFR_{FIR}, $SFR_{Br\gamma}$, $SFR_{RC\text{-}N}$, and $SFR_{RC\text{-}T}$) from these tracers and the aperture over which it applies. From these values, we make a best estimate for SFR_{CO}, the extinction-corrected SFR within the radius (R_{CO}) over which CO emission is detected in the moment maps. In the case of NGC 470, NGC 2782, NGC 4102, NGC 4536, and NGC 4569, we consider $SFR_{RC\text{-}N}$ to be a reasonable estimate for SFR_{CO} since the RC maps show that most of the RC emission is concentrated within R_{CO}. For the remaining galaxies NGC 3504, NGC 3351, and NGC 4314, R_{RC}/R_{CO} is 0.6, 1.7, and 6.0, respectively. In NGC 3504, $SFR_{RC\text{-}N}$ is a reasonable approximation of the SFR within R_{CO} (1300 pc) because the Hα map shows that more than 90% of the Hα flux within R_{CO} originates from the inner 800 pc radius. In the case of NGC 3351, R_{CO} is ~600 pc, which is close to $R_{Br\gamma} \sim 500$ pc. We therefore adopt SFR_{CO} as 0.5 $M_\odot$ yr^{-1} based on the Brγ estimates. In the case of NGC 4314, we consider $SFR_{RC\text{-}N} \sim 0.1\,M_\odot$ yr^{-1} within $R_{RC} \sim 3600$ pc as an upper limit to the SFR within $R_{CO} \sim 600$ pc.

Table 8 shows the resulting R_{CO}, SFR_{CO}, and mass of molecular hydrogen (M_{H2}) within this radius. The resulting circumnuclear SFR ranges from 3 to 11 $M_\odot$ yr^{-1} in the starbursts and from 0.1 to 2 $M_\odot$ yr^{-1} in the nonstarbursts. It is evident that while nonstarbursts such as NGC 4569 and NGC 6951 and starbursts such as NGC 4102, NGC 4536, and NGC 2782 all host several times 10^9 $M_\odot$ of molecular hydrogen, their SFRs are substantially different. A similar comparison applies between the starburst NGC 470 and the nonstarbursts NGC 3351 and NGC 4314, which host several times 10^8 $M_\odot$ of molecular hydrogen.

8. COMPARISON OF MOLECULAR GAS IN THE STARBURSTS AND NONSTARBURSTS

Table 8 shows that barred galaxies with comparable amount of molecular gas in the inner 1–2 kpc radius can show an order of magnitude range in the average SFR per unit mass of gas (SFR/M_{H2}) within this region. Among galaxies that host several times 10^9 $M_\odot$ of molecular hydrogen in the inner 2 kpc, starbursts such as NGC 4102, NGC 4536, and NGC 2782 have an average SFR/M_{H2} of order a few $\times$ 10^{-9} yr^{-1}, while nonstarbursts NGC 4569 and NGC 6951 have $SFR/M_{H2} \sim$ a few $\times$ 10^{-10} yr^{-1}. We now turn to a comparison of the circumnuclear molecular gas in the barred starbursts and nonstarbursts with the overall goal of understanding why they have such different SFRs per unit mass of gas (SFR/M_{H2}) in the inner few kiloparsecs.

While we focus here on a comparison of the starbursts and nonstarbursts (Figs. 3, 5, 6, and 7), we refer any interested reader to § 11 for a description of each individual galaxy. Figures 3*a* and 3*b* show a wide variety of molecular gas morphologies, including relatively axisymmetric annuli or disks (starbursts NGC 4102, NGC 3504, NGC 4536, and NGC 470, and nonstarburst NGC 4314), elongated double-peaked and spiral morphologies (starburst NGC 2782 and nonstarbursts NGC 3351 and NGC 6951), and highly extended distributions (nonstarburst NGC 4569). In all of the sample galaxies (Figs. 3*a* and 3*b*) except for the nonstarburst NGC 4569, the molecular gas is concentrated in the inner kiloparsec radius. Figure 5 compares the spatial distribution of SF activity (*gray scale*) and molecular gas (CO *contours*). The *x* and *y* axes represent respectively M_{H2} and SFR/M_{H2}, as defined in Table 8. In the case of NGC 4102, NGC 2782, and NGC 6951, we show the SF activity with existing high-resolution (1.″0–1.″5) 1.49 and 4.89 GHz RC maps. Strictly speaking, in the case of NGC 6951 the RC map shows not just the star-forming ring of 4″ (360 pc) radius, but also the Seyfert nucleus in the inner 1″ (90 pc). For the remaining galaxies in Figure 5, we use high-resolution (1.″0–1.″5) Hα maps, as there are no RC maps of resolution comparable to the CO. Our conclusions are given below.

8.1. *The Type I Nonstarburst NGC 4569*

The nonstarburst NGC 4569 differs from the other sample galaxies in that it has a highly extended molecular gas distribution with complex kinematics and large line widths of ~150 km s^{-1}. These properties of NGC 4569 are illustrated in Figures 6*a*–6*d*. A large fraction of the gas lies outside the inner kiloparsec radius and extends out to a radius of 20″ (1.7 kpc), at a P.A. (~15°) similar to that of the large-scale stellar bar (Figs. 6*a* and 6*b*). The extended gas in NGC 4569 has highly noncircular kinematics, as shown by the *p-v* plots along the kinematic major and minor axes (Figs. 6*c* and 6*d*). Along the kinematic major axis, velocities are generally positive (i.e., above the systemic value of −235 km s^{-1}) on the northeastern side, and negative on the southwest side. However, at a radius of 5″ (400 pc), near the feature marked "N1" in Figure 6*b*, the velocities change from +100 km s^{-1} to a forbidden velocity of −75 km s^{-1}. This indicates the presence of noncircular motions caused by in-plane azimuthal streaming motions or/and vertical motions out of the plane.

As outlined in § 3, NGC 4569 shows signs of optical and NIR asymmetries suggestive of a recent tidal interaction or minor merger, and it also hosts a large-scale stellar bar. Thus, we suggest that the extended gas in NGC 4569, which is generally elongated along the bar and shows strong streaming motions, is responding to gravitational torques from both the interaction and the (induced or spontaneous) stellar bar. Taken together, the optical, NIR, and CO properties of NGC 4569 suggest that it is in the early phases of bar-driven/tidally driven gas inflow. NGC 4569 is reminiscent of NGC 7479, which hosts large amounts of gas with noncircular kinematics along a large-scale stellar bar and shows evidence of a minor merger (Laine & Heller 1999). However, the gas kinematics in NGC 4569 look more disturbed in the inner 400 pc than in NGC 7479.

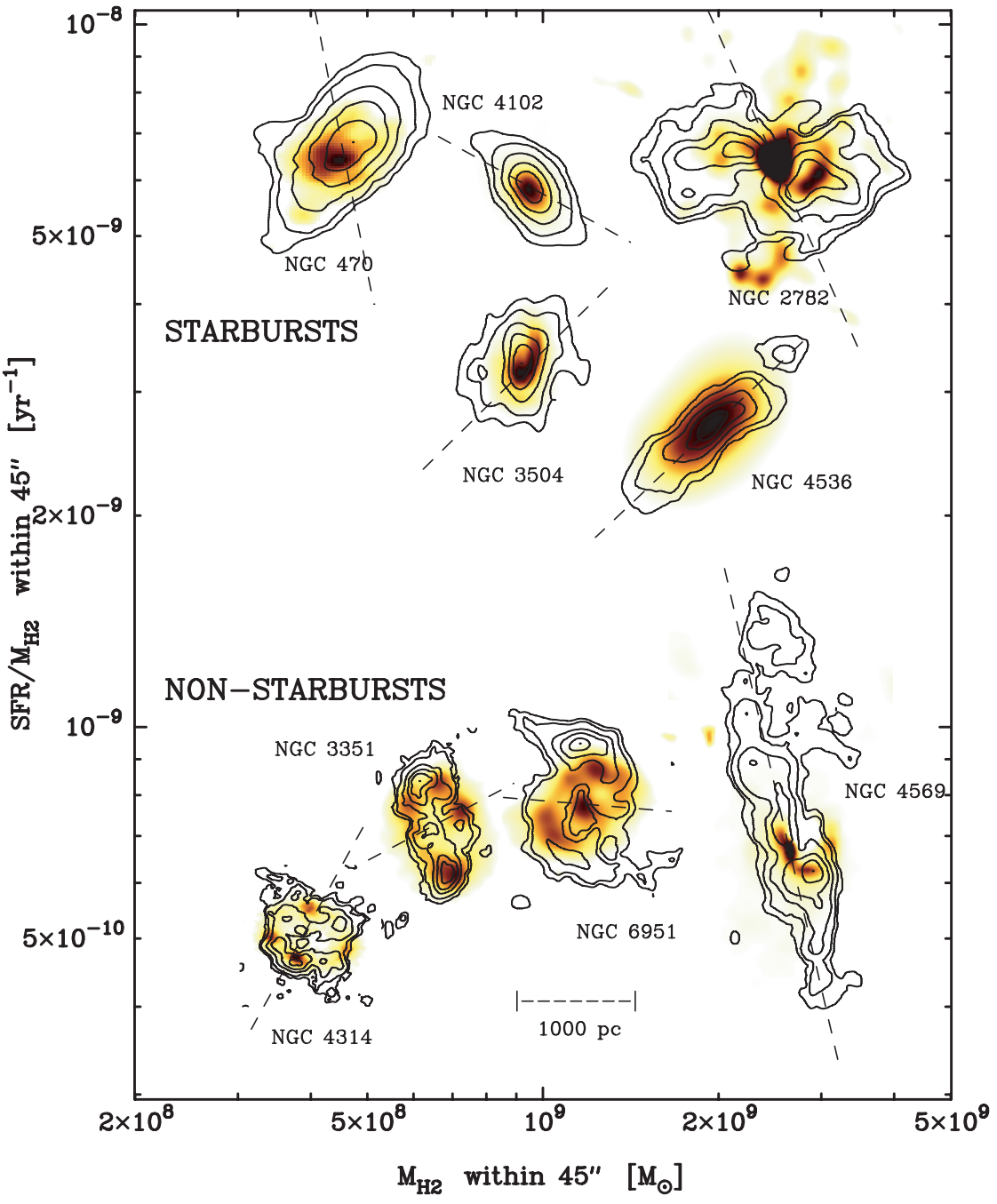

FIG. 5.—Distribution of molecular gas and SF in the barred starbursts and nonstarbursts. In the SFR/M_{H2} vs. M_{H2} plane, the CO intensity (*contours*) is overlaid on the 1.5 or 4.9 GHz radio continuum map (*gray scale*) of NGC 4102, NGC 2782, and NGC 6951 and on the Hα map for the other galaxies. The gray scale traces the SF activity, and in the case of NGC 6951, it also shows the Seyfert 2 nucleus in the inner 100 pc. The Hα and RC maps have a resolution of 1.″0–1.″5. The synthesized CO beam is typically 2″ or 100–200 pc. The dotted line is the P.A. of the large-scale stellar bar/oval. The contour levels plotted are specified in Table 10.

There is intense SF in the central 2″ (170 pc) radius, but the gas that is extended along the bar and has disturbed kinematics shows no appreciable SF. The properties of NGC 4569 stand in sharp contrast to the starburst NGC 4102, where most of the circumnuclear molecular gas has piled up in the inner 4″ (340 pc) radius, shows predominantly circular kinematics, and is undergoing intense SF. The low SF efficiency in NGC 4569 is likely related to the fact that large velocity gradients and shear in gas streaming along the bar can prevent clouds from being self-gravitating. In addition, gas moving in a bar potential can experience large tidal forces (Elmegreen 1979; Kenney & Lord 1991) and tidal heating (Das & Jog 1995), which slow down gravitational collapse. Several other galaxies show such low SF per unit mass of gas along their bars, e.g., NGC 7723 (Chevalier & Furenlid 1978), NGC 1300 and NGC 5383 (Tubbs 1982), NGC 7479 (Laine et al. 1999), or M83, where the ratio of UV to CO luminosities is unusually low despite abundant CO (Handa et al. 1991).

In summary, we therefore suggest that the low SFR per unit gas mass of the nonstarburst NGC 4569 over the inner few kiloparsecs is due to the fact that it is in the early stages of bar-driven/tidally driven gas inflow, where most of its molecular gas has an extended distribution, highly noncircular kinematics, and an

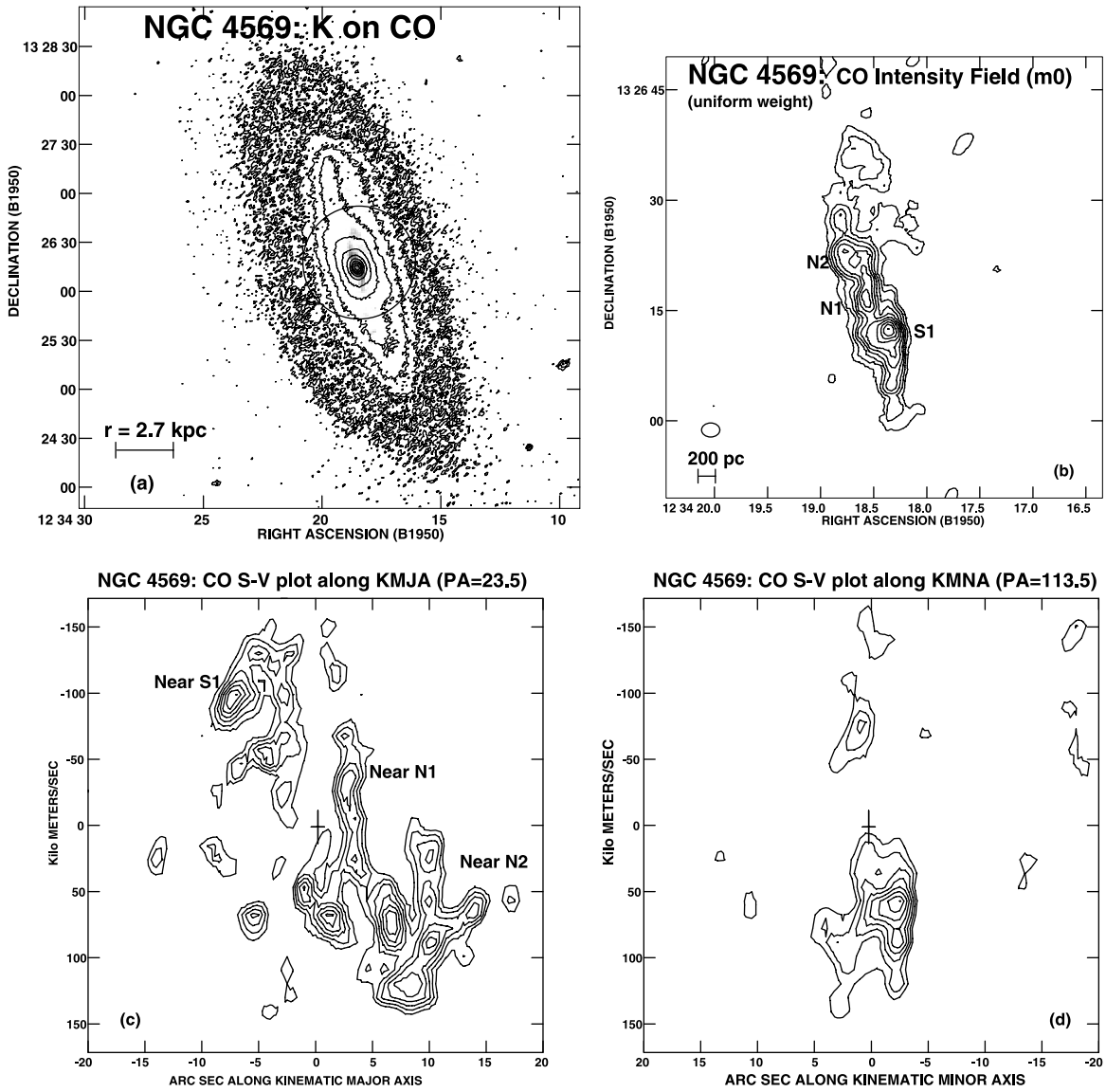

FIG. 6.—Gas distribution and kinematics in NGC 4569. (*a*) The *K*-band image (*contours*) with a field of view of 5′ (25.9 kpc) shows an asymmetric stellar bar. The overlaid circle shows the 65″ HPBW of the CO interferometric observations. The CO distribution inside the beam is shown in gray scale. (*b*) The uniformly weighted (2″.65 × 2″.01 or 223 pc × 169 pc) CO total intensity map in the central 6″ (5.0 kpc) shows an extended molecular gas distribution in NGC 4569. Contour levels plotted are 3.20 Jy beam^{-1} km s^{-1} × (1, 2, 3, 4, 5, 6, 7, 8, 9, 10). The gas extends out to a large (20″ or 1.7 kpc) radius and is elongated along the direction of the large-scale stellar bar. (*c*, *d*) The *p-v* plots along the kinematic major and minor axes. The molecular gas extends out to a 2 kpc radius and shows very disturbed kinematics. Along the kinematic major axis, velocities are generally positive (i.e., above the systemic value) on the northeastern side. However, at a radius of 5″ (400 pc), near the feature marked "N1" in (*b*), the velocities change from about +100 km s^{-1} to a forbidden velocity of −75 km s^{-1}.

associated large local shear that is not conducive to SF. The barred galaxy NGC 7479 studied by Laine et al. (1999) may also be in this early evolutionary phase. In NGC 7479, only low levels of SF are seen along the bar despite the presence of several $\times 10^9\ M_\odot$ of molecular gas in a dust lane along the bar (Laine et al. 1999). This gas shows large noncircular motions, a large velocity gradient, and a projected velocity gradient of at least 100 km s^{-1} (Laine et al. 1999). We henceforth use the term "type I nonstarburst" to denote this kind of system, where a large fraction of the molecular gas is still inflowing toward the inner kiloparsec, along the leading edges of the bar, exhibiting large noncircular motions and not forming stars efficiently.

8.2. *The Starbursts and Type II Nonstarbursts*

The remaining starbursts (NGC 4102, NGC 3504, NGC 4536, NGC 470) and nonstarbursts (NGC 6951, NGC 3351, NGC 4314) in our sample do not show such extreme kinematics or extended gas distributions as NGC 4569. In all of them, the molecular gas detected is concentrated within the inner kiloparsec radius, and the velocity field in the inner 500 pc radius is generally dominated by circular motions, with occasional weaker noncircular components (see § 11 for details). Most of the circumnuclear molecular gas seems to have reached the inner kiloparsec radius of the bar, and only a small fraction of it seems to be still inflowing along the stellar bar. The latter gas component shows up in the form of faint gas streams that extend out and intersect the dust lanes on the leading edges of the large-scale bar and show noncircular motions. Such gas streams are seen clearly in nonstarburst NGC 6951 (Figs. 15*a* and 15*b*) and also at fainter levels in NGC 3351 (Figs. 15*c* and 15*d*), NGC 4314 (Figs. 15*e* and 15*f*), and starburst NGC 4102 (Figs. 14*a* and 14*b*). We conclude that in contrast to NGC 4569, the remaining

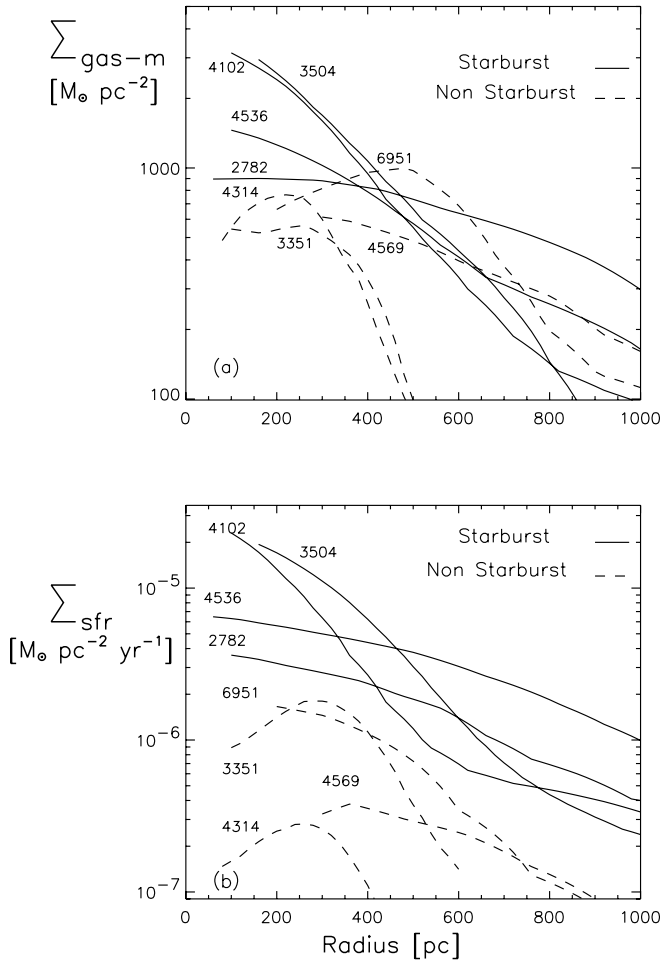

FIG. 7.—(*a*, *b*) Azimuthally averaged molecular gas surface density ($\Sigma_{\rm gas\text{-}m}$) and the SFR per unit area ($\Sigma_{\rm SFR}$). The extinction-corrected profiles are convolved to a similar resolution of 100–200 pc for all the galaxies. Quantities are plotted starting at a radius of ≥half the size of the synthesized beam (typically 2″ or 150 pc). Most of the starbursts have developed larger molecular gas surface densities (1000–3500 $M_\odot$ pc^{-2}) in the inner 500 pc radius than the nonstarbursts, for a given CO-to-H_2 conversion factor. In the inner 500 pc radius of the starbursts, both $\Sigma_{\rm gas\text{-}m}$ and $\Sigma_{\rm SFR}$ increase toward the center.

barred starbursts and nonstarbursts seem to be in significantly later stages of bar-driven inflow, where most of the molecular gas has already settled into the inner kiloparsec of the barred potential and no longer shows extreme noncircular motions. We henceforth refer to these kinds of nonstarbursts as "type II nonstarbursts."

What is the difference between the starbursts and type II nonstarbursts? To answer this question, we use the two-dimensional distribution of SF and gas in Figure 5, as well as the azimuthally averaged gas and SFR surface densities in Figures 7*a* and 7*b*. Figure 7*a* shows the radial variation of the deprojected azimuthally averaged molecular gas surface density $\Sigma_{\rm gas\text{-}m}$ derived in § 5. In order to display meaningful values, quantities are plotted starting at a radius ≥ half the size of the synthesized CO beam, which is typically 2″ or 150 pc. Figure 7*b* plots the azimuthally averaged molecular gas surface density SFR per unit area ($\Sigma_{\rm SFR}$) in the galactic plane as a function of radius. We find that the starbursts show larger gas surface densities (1000–3500 $M_\odot$ pc^{-2}) in the inner 500 pc radius compared to the type II nonstarbursts for a given CO-to-H_2 conversion factor. In Figure 7*a*, the type II nonstarbursts have peak $\Sigma_{\rm gas\text{-}m}$ reaching only 500–950 $M_\odot$ pc^{-2}. We also note from Figures 6*a* and 6*b* that in the central 600 pc radius, $\Sigma_{\rm gas\text{-}m}$ and $\Sigma_{\rm SFR}$ follow each other more closely in the case of the starbursts.

Is the presence of apparently higher gas surface densities in the starbursts a real effect? We can rule out artifacts caused by resolution effects since we have similar linear resolution (in parsecs) for starbursts and nonstarbursts with comparable circumnuclear molecular gas content (e.g., NGC 4102 and NGC 3504 vs. NGC 6951, or NGC 2782 and NGC 4536 vs. NGC 4569). Another concern is that the higher $\Sigma_{\rm gas\text{-}m}$ in the starbursts may be due to an increase in CO emissivity caused by the higher temperatures associated with the intense SF. However, potential variations in CO emissivity cannot account for the observed differences in $\Sigma_{\rm gas\text{-}m}$ since CO peaks do not coincide with the Hα and RC peaks in several galaxies, e.g., NGC 6951, NGC 2782, and NGC 3351 (Fig. 5). Thus, the starbursts appear to have an intrinsically larger molecular gas surface density in the central 500 pc than the nonstarbursts. This difference of a factor of 3–4 in $\Sigma_{\rm gas\text{-}m}$ can in turn lead to large differences in the SF if gas in the starbursts is above a critical density for SF while a large part of the gas in the nonstarbursts is subcritical. We address this possibility quantitatively in § 9 by comparing $\Sigma_{\rm gas\text{-}m}$ to different theoretical critical densities that are believed to be relevant for the onset of SF.

9. THEORETICAL MODELS OF STAR FORMATION APPLIED TO CIRCUMNUCLEAR STARBURSTS AND TYPE II NONSTARBURSTS

We compare the observed circumnuclear gas surface density $\Sigma_{\rm gas\text{-}m}$ to the critical density relevant for the onset of SF with the overall goal of understanding some of the differences between the starbursts and type II nonstarbursts. In particular, we consider theoretical scenarios that assume that the onset of gravitational or axisymmetric instabilities (Safronov 1960; Toomre 1964; Goldreich & Lynden-Bell 1965; Elmegreen 1979) is relevant for the growth of clouds and the onset of SF. Such models have achieved a fair degree of empirical success in the outer disks of Sa–Sc spirals and gas-rich E and S0s (Kennicutt 1989, 1998b; Eder 1990). Extensions of such models to include magneto-Jeans instabilities have also been developed (Kim et al. 2002).

For a thin differentially rotating gas disk, support against gravitational instabilities is provided by pressure forces on small scales, and by Coriolis forces from rotation on large scales. One can show that axisymmetric instabilities set in when the gas surface density $\Sigma_{\rm gas}$ exceeds a critical density such that the Safronov (1960)/Toomre (1964) Q parameter falls below 1, where

$$Q = \frac{\Sigma_{\rm crit}}{\Sigma_{\rm gas}} = \frac{\alpha\kappa\sigma}{\pi G\Sigma_{\rm gas}} \leq 1. \qquad (10)$$

Here ω is the angular frequency, $\Sigma_{\rm gas}$ is the gas surface density, σ is the gas velocity dispersion, κ is the epicyclic frequency, and G is the gravitational constant. For an infinitely thin disk, α is 1, but for disks of finite thickness, α is somewhat larger (Larson 1985). Empirically, Kennicutt (1989) found that α is ~0.7 in the outer disks of Sc spirals. A two-fluid disk made of both gas and stars is always more unstable and will have a lower α than a purely gaseous or stellar one-fluid disk (Jog & Solomon 1984; Elmegreen 1995).

We discuss the gravitational instability models in the context of the type II nonstarbursts NGC 4314, NGC 3351, and NGC 6951 and the starbursts NGC 4102, NGC 4536, and NGC 3504. We cannot apply these simply axisymmetric models to other

sample galaxies since they have highly nonaxisymmetric gas distributions (e.g., the starburst NGC 2782 and type I nonstarburst NGC 4569) and noncircular kinematics (e.g., NGC 4569). We ignore the contribution of atomic H I because we have limited high-resolution H I data for our sample galaxies and, furthermore, molecular hydrogen is believed to dominate the ISM in the inner kiloparsec of spirals (e.g., Scoville & Sanders 1987; Tacconi & Young 1986).

A more vicious problem is to get a good estimate of the velocity dispersion σ in the central $2''$, especially when the $2''$ CO beam encompasses a steeply rising rotation curve. In the latter case, beam smearing artificially increases the observed σ and to a lesser degree impacts κ and $\Sigma_{\rm gas}$ in ways that depend on the intrinsic intensity and velocity field (Jogee 1999). Given that corrections for beam smearing are model-dependent and not necessarily unique, we have decided not to apply any such corrections, and instead perform the instability analyzes (Fig. 8) only for radii exceeding $2''$, where the effect of beam smearing is much less severe. In nonstarbursts and starbursts alike, we therefore present results over radii of $\sim 2''$–$8''$ (Fig. 8). The lower limit of $2''$ corresponds to 180 pc for NGC 6951, NGC 4102, and NGC 4536, and to 100 pc for NGC 4314 and NGC 3351. We summarize our results as follows.

1. *Type II nonstarburst NGC 4314*.—H II regions are concentrated within an annulus between a radius of $5''$ and $7''$ (240 and 400 pc), where $\Sigma_{\rm gas}$ is $\sim 800\ M_\odot\ {\rm pc}^{-2}$ (Fig. 8). Interior to this annulus there are no H II regions, although $\Sigma_{\rm gas}$ drops by only a factor of 2–3 (Fig. 8). This lack of SF activity is not an artifact caused by extinction in the Hα image or by resolution effects since neither the $J-K$ image (Friedli et al. 1996) nor the high-resolution *HST* images (Benedict et al. 1996) show elevated levels of dust or young stars at $r < 250$ pc. Thus, SF appears truly suppressed interior to the annulus of H II regions. The instability analysis (Fig. 8) shows that Q reaches its lowest value, between 1 and 2, in the star-forming annulus between $r = 5''$ and $7''$ (240 and 400 pc) and that it rises sharply at lower and higher radii. At $r \geq 7''$, where we cannot measure σ, we adopted a lower limit of 10 km s^{-1} based on the fact that a relatively constant value of 10–6 km s^{-1} has been measured in the outer disks of spirals (e.g., Dickey et al. 1990). Thus, values estimated for Q at $r \geq 7''$ outside the SF annulus are lower limits, and the true rise in Q is likely to be even sharper than shown in Figure 8. Interior to the star-forming annulus, between $r = 2''$ and $5''$ (100–240 pc), Q increases by more than a factor of 3, indicating highly subcritical gas densities. It is unlikely that this rise in Q is primarily due to beam smearing because the observed σ increases by at most 1.5 interior to the SF annulus. (The mean value of $\sigma = 25$ km s^{-1} inside the SF ring and 15 km s^{-1} in the ring).

2. *Type II nonstarburst NGC 3351*.—The SF activity is concentrated within an annulus between a radius of $6''$ and $9''$ (300 and 450 pc), where $\Sigma_{\rm gas}$ is $\sim 550\ M_\odot\ {\rm pc}^{-2}$ (Fig. 8). At lower radii, between $2''$ and $6''$ (100 and 450 pc), there is a large amount of molecular gas and $\Sigma_{\rm gas}$ shows no significant change. Yet no H II regions are seen (Fig. 8). The absence of observed SF activity at $r < 6''$ is not caused by extinction since near-infrared K-band observations of NGC 3351 show several hot spots (likely due to young K supergiants) in the ring of H II regions, but a relatively smooth distribution suggestive of older stars farther in (Elmegreen et al. 1997). We find that in NGC 3351 Q reaches its minimum value of ~ 1.5 in the annulus of H II regions between a radius of $6''$ and $9''$ (300 and 450 pc; Fig. 8). Farther in, between a radius of $2''$ and $6''$ (100 and 450 pc), Q rises sharply to ~ 6, suggesting subcritical gas densities. We again note that this increase in Q by a factor of >3 is not primarily due to beam smearing since the observed σ does not show a similar increase; σ has a mean value of 20 km s^{-1} in the SF ring and 25 km s^{-1} inside it.

3. *Type II nonstarburst NGC 6951*.—Here a similar trend in the Q parameter exists. The massive CO peaks at a radius of $6''$ (550 pc) host a local molecular gas surface density of 2000 $M_\odot$ pc^{-2} and an azimuthally averaged $\Sigma_{\rm gas}$ of 1000 $M_\odot$ pc^{-2} (Fig. 8). Yet, the CO peaks are not associated with SF in either the Hα or RC maps. Instead, SF is concentrated in a ring of radius $\sim 3''$ (300 pc). Kohno et al. (1999) find that Q is close to 1 in the star-forming annulus.

4. *The starbursts NGC 4102 and NGC 4536*.—The circumnuclear SF in these starbursts is distributed over a wide annulus between 100 and 700 pc. Although the ground-based Hα or RC images (e.g., Fig. 5) may give the misleading impression that SF extends all the way into the center, *HST* images of both galaxies show a smooth distribution of old stars within the central 100 pc ($1''$) radius. Adopting the same approach for the starbursts NGC 4102 and NGC 4536 as for the nonstarbursts, we perform the instability analysis from $r \sim 2''$ to $8''$ (Fig. 8). As before, we exclude the central $r \sim 2''$ radius, where the effect of beam smearing is severe. We also exclude larger radii ($r > 8''$) where there are faint gas streams that connect to the large-scale dust lanes on the leading edges of the bar because the Toomre analysis is not valid for such nonaxisymmetric gas distributions.

The instability analysis (Fig. 8) shows that in the starbursts NGC 4102 and NGC 4536, the Toomre Q parameter remains $\sim$1–2 from $r \sim 2''$–$8''$ (200–700 pc) in the region of SF despite a factor of 2–3 variation in σ and a factor of 10 variation in both the gas surface density $\Sigma_{\rm gas}$ and the epicyclic frequency κ. Indeed, between a radius of 200 and 700 pc, σ ranges from 40 to 15 km s^{-1}, $\Sigma_{\rm gas}$ from 2200 to 200 $M_\odot$ pc^{-2}, and κ from 1500 to 200 km s^{-1} kpc^{-1}. A value of $Q \sim 1$ is also found in the starburst NGC 3504 by Kenney et al (1993). Furthermore, inspection of Figure 8 shows that the $Q \sim 1$–2 annulus spans $\sim$450 pc (e.g., 250–700 pc) in the starbursts NGC 4102 and NGC 4536, but only $\sim$150 pc (e.g., 300–450 pc) in the nonstarbursts NGC 4314 and NGC 3351. It thus appears that the annulus over which Q remains $\sim$1–2 is 3 times wider in the starbursts than in the nonstarbursts, suggesting that the former host a larger amount of gas that is close to the critical density.

5. *Overall trends*.—The analyzes in results 1–4 suggest that the Toomre Q parameter remains $\sim$1–2 in the region of SF despite the large dynamic range in molecular gas properties, namely, a factor of a few variation in σ and an order of magnitude variation in the gas surface density $\Sigma_{\rm gas}$ and the epicyclic frequency κ. It is true that the analyzes involve many uncertain quantities such as the CO-to-H_2 conversion factor and should, therefore, be taken with a grain of salt. However, with such a large variation in quantities such as $\Sigma_{\rm gas}$ and κ, Q could easily have ended up having almost any value, and the fact that it remains close to 1 can hardly be fortuitous. Instead, the evidence presented strongly suggests that the onset of gravitational instabilities as characterized by Q plays an important role in controlling the onset of SF in the inner kiloparsec of spirals. At first sight, this may seem surprising since large-scale gravitational instabilities have been invoked for the collapse of atomic gas into molecular clouds within the outer disk of galaxies, but molecular gas in the inner kiloparsec is already in the form of clouds. However, large-scale gravitational instabilities may be relevant for SF even in the inner kiloparsec because they help to aggregate molecular clouds into large complexes where the clouds can thereafter grow through local processes involving accretion and

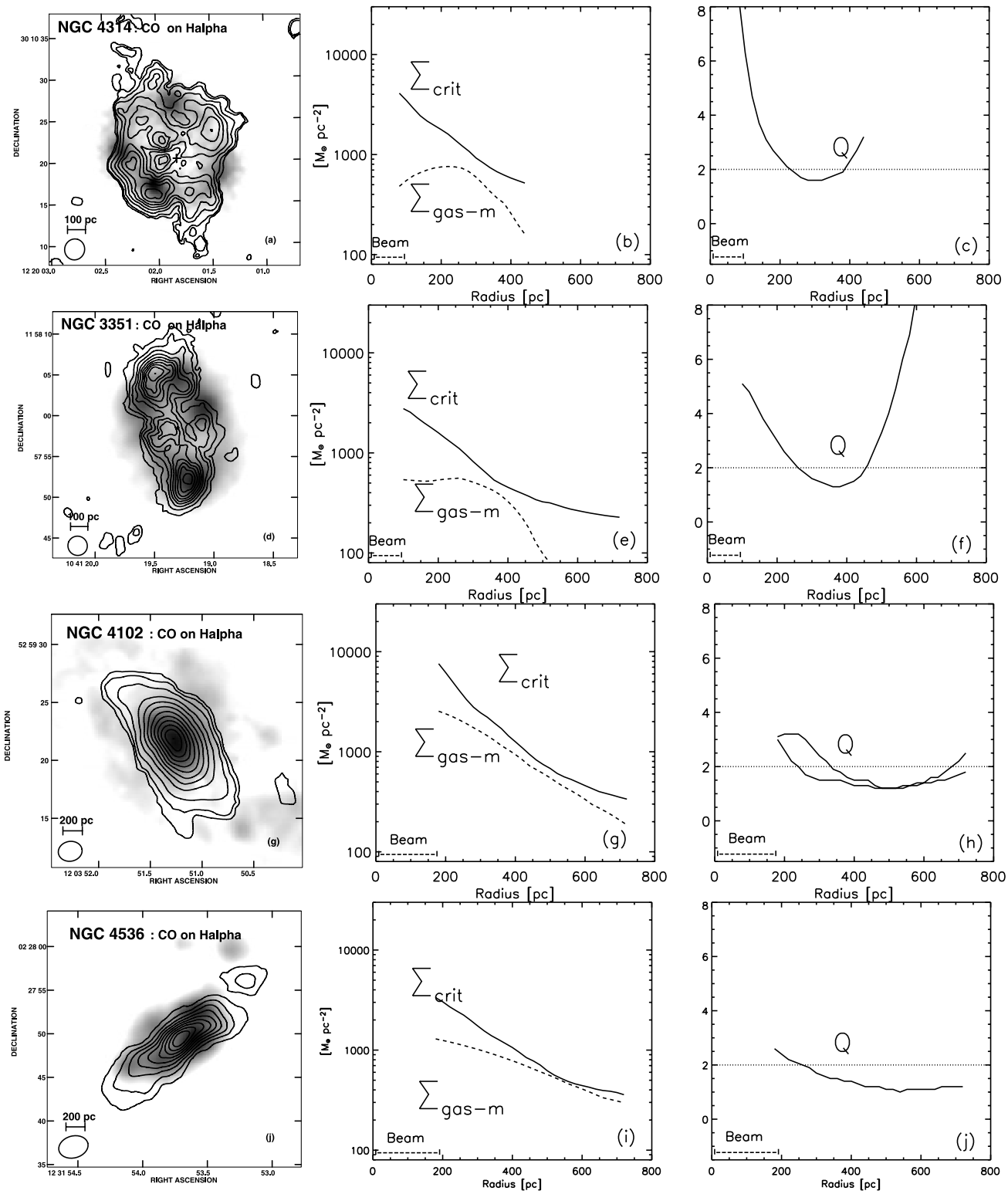

FIG. 8.—Comparison of the gas density with the Toomre critical density in the nonstarbursts and starbursts. *Left*: CO distribution (*contours*) on the Hα (*gray scale*) for the nonstarbursts NGC 4314 and NGC 3351 and the starbursts NGC 4102 and NGC 4536. *Middle*: Molecular gas surface density $\Sigma_{\rm gas\text{-}m}$ and the critical density ($\Sigma_{\rm crit} = \alpha\kappa\sigma/\pi G$) for the onset of gravitational instabilities assuming $\alpha = 1$. Quantities are plotted starting at a radius equal to the CO beam size ($\sim$2″). *Right*: Toomre Q parameter ($\Sigma_{\rm crit}/\Sigma_{\rm gas}$). The horizontal line denotes the value of Q in the outer disk of spirals where Kennicutt (1989) finds $\alpha = 0.7$. In the nonstarbursts NGC 4314 and NGC 3351, H II regions are concentrated in a gas-rich annulus of radius 350 pc (7″), while farther in, the star formation activity drops sharply despite large gas surface densities above 400 $M_\odot$ pc^{-2}. In these nonstarbursts, Q reaches its lowest value (1–2) in the ring of H II regions, while at lower radii Q increases to $\sim$6, suggesting subcritical gas densities. In the starbursts NGC 4102 and NGC 4536, Q remains remarkably close to 1–2 over a wide region, between a radius of 250 and 700 pc, although the gas surface density and the epicyclic frequency both vary by nearly an order of magnitude.

TABLE 9
PRIMARY-BAR PROPERTIES AND DYNAMICAL RESONANCES

NGC Number (1)	Bar (2)	ϵ_1 (deg) (3)	P.A.$_1$ (deg) (4)	a_1 (kpc) (5)	$M_{\rm gas\text{-}m}$ ($M_\odot$) (6)	$\frac{M_{\rm gas\text{-}m}}{M_{\rm dyn}}$ (7)	Ω_p (km s^{-1} kpc^{-1}) (8)	$R_{\rm OILR}$ (pc) (9)	$R_{\rm IILR}$ (pc) (10)
470.....	AB	0.55[a]	14[a]	4.8[a]	2E8	30	...	...	...
3504.....	AB	0.58[b]	135[b]	3.0[c]	8E8	20	<76	>900	<200
4102.....	AB	0.45[c]	62[c]	1.8[c]	8E8	25	<115	>500	<250
4536.....	AB	0.40[b]	140[b,d]	3.1[d]	1E9	30	<50	>800	<200
3351.....	B	0.57[e]	115[d]	2.2[d,e]	2E8	17	<85	>300	<300
3359.....	B	0.68[e]	24[d]	2.9[e]	...	...	...	...	...
4314.....	B	0.69[a]	143[a]	3.6[a]	2E8	9	<78	>700	<200
4569.....	AB	...	15[c]	...	2E8	...	...	...	...
6951.....	AB	0.59[a]	85[a]	5.2[a]	3E8	21	<43	>650	<300

NOTES.—Col. (2): Bar type from RC3. B denotes a strong bar, and AB a bar of intermediate strength. Cols. (3)–(5): Ellipticity, position angle, and semimajor axis of the large-scale stellar bar. Col. (6): Molecular gas mass enclosed within a 300 pc radius. A standard CO-to-H_2 conversion factor and a solar metallicity are assumed. Col. (7): Ratio of molecular gas mass to dynamical mass within a 300 pc radius. Col. (8): Upper limit on Ω_p, the primary bar pattern speed. Col. (9): Upper limit on $R_{\rm OILR}$, the radius of the outer inner Lindblad resonance. Col. (10): Lower limit on $R_{\rm IILR}$, the radius of the inner inner Lindblad resonance.

[a] Friedli et al. (1996).
[b] Pompea & Rieke (1990).
[c] This work.
[d] Shaw et al. (1995).
[e] Martin (1995).

collisions (e.g., Kwan 1979; Scoville et al. 1986; Gammie et al. 1991; Elmegreen 1990).

Results 1–4 also suggest at least a partial explanation for the differences in SFR per unit mass of gas between the nonstarbursts and starbursts. In both type II nonstarbursts and starbursts, the Q parameter reaches its minimum value of $\sim$1–2 in the annuli of SF. However, the annulus over which Q remains $\sim$1–2 is 3 times wider in the starbursts than in the nonstarbursts, suggesting that starbursts host a larger amount of gas that is close to the critical density. Inside and outside the annuli of SF, the type II nonstarbursts host large gas concentrations where gas densities are well below $\Sigma_{\rm crit}$ ($Q \gg 2$), and SF appears inhibited.

10. BAR PATTERN SPEEDS AND DYNAMICAL RESONANCES OF THE BAR

A barred potential is made up of different families of periodic stellar orbits characterized by a (conserved) Jacobi energy $E_{\rm J}$, a combination of energy and angular momentum (e.g., Binney & Tremaine 1987). The most important families are those aligned with the bar major axis (so-called x_1 orbits) or with its minor axis (x_2 orbits) (Contopoulos & Papayannopoulos 1980). The x_1 family extends between the center and the bar's corotation radius. If the central mass concentration of a bar is large enough, it can also develop one or more inner Lindblad resonances (ILRs). The exact locations and even the number of ILRs can be inferred reliably from nonlinear orbit analysis (e.g., Heller & Shlosman 1996) based on the knowledge of the galactic potential. The abrupt change in orientation by $\pi/2$ at each resonance is restricted to (collisionless) stellar orbits. The gas-populated orbits can change their orientation only gradually due to shocks induced by the finite gas pressure. The gas response to bar torquing leads to the formation of large-scale offset shocks and a subsequent gas inflow. The latter stalls in the inner few 100 pc because shocks associated with the bar weaken, and gravitational torques in the vicinity of ILRs may even reverse (e.g., Combes & Gerin 1985; Shlosman et al. 1989; Athanassoula 1992).

Here we use the CO, optical, and NIR data of the sample galaxies to constrain two fundamental properties of their stellar bar: its pattern speed Ω_p and the location of its dynamical resonances. The pattern speed influences the interaction of the bar with the dark matter halo (e.g., Debattista & Sellwood 2000; Athanassoula 2002; Berentzen et al. 2005) and the location of its resonances. We use two empirical methods:

1. *Kinematic method based on the epicyclic approximation.*—For a weak bar, the potential can be expressed as the linear sum of an axisymmetric term and a smaller nonaxisymmetric term, and epicycle theory can be used to solve for the equations of motion of a star. In such a case, simple relationships exist between the location of its resonances and dynamical frequencies, such as Ω_p, Ω, and κ. We derive Ω and κ from the CO and Hα rotation curves as described in § 5, bearing in mind that uncertainties exist in regions where there are noncircular motions. We fit ellipses to the NIR and optical images in order to estimate the location of the bar end (e.g., Jogee et al. 1999, 2004a). Next, we set upper limits on the pattern speed Ω_p by assuming that a bar ends inside or at the corotation resonance (CR), where $\Omega = \Omega_p$. This widely used assumption is justified by the fact that between the ultraharmonic resonance and CR, chaotic orbits dominate, while beyond the CR, the orbits become aligned perpendicular to the bar. We derive upper limits on Ω_p in the range of 43–115 km s^{-1} kpc^{-1} across the sample (Table 9; Figs. 9*a* and 9*b*).

At the ILRs, there is a match between the natural frequency of radial oscillations (κ), and the forcing frequency ($\Omega - \Omega_p$),

$$\Omega - \Omega_p = \pm\kappa/2, \tag{11}$$

where Ω is the angular frequency and Ω_p is the bar pattern speed. For a weak bar, if the peak of $\Omega - \kappa/2$ exceeds Ω_p (Figs. 9*a* and 9*b*), then one or more ILRs must exist. This condition is satisfied in the starbursts NGC 4102, NGC 4536, and NGC 3504, and in the nonstarbursts NGC 4314, NGC 6951, and NGC 3351. We use the upper limit on Ω_p in Figures 9*a* and 9*b* to derive lower and upper limits, respectively, for the radius of the outer inner Lindblad resonance ($R_{\rm OILR}$) and the radius of the inner inner Lindblad resonance ($R_{\rm IILR}$). These are shown in Table 9.

2. *Method based on the morphology of circumnuclear dust lanes.*—In the presence of x_2 orbits associated with ILRs, the

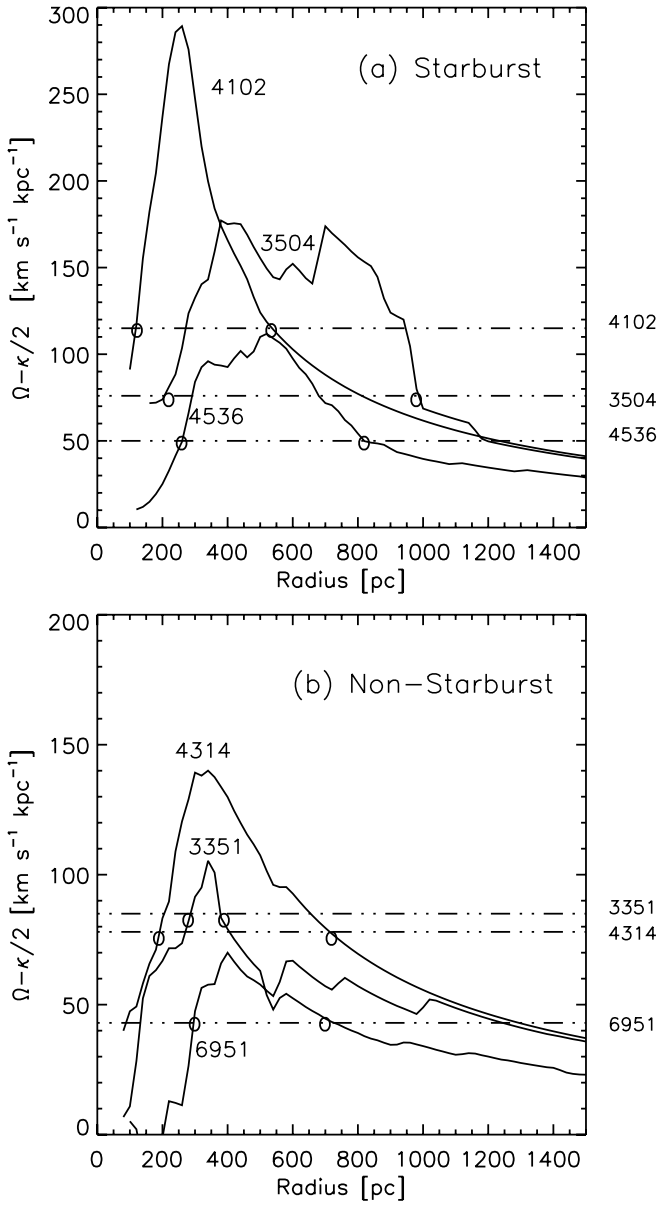

FIG. 9.—ILRs in the barred starbursts and nonstarbursts. The quantity $\Omega - \kappa/2$ is plotted against radius for select (*a*) starbursts and (*b*) nonstarbursts. The bar pattern speed Ω_p is drawn as horizontal lines and estimated by assuming that the corotation resonance is near the end of the large-scale stellar bar (see Table 9). Under the epicycle theory for a weak bar, the intersection of $\Omega - \kappa/2$ with Ω_p defines the locations of the ILRs. In these systems, the circumnuclear gas is concentrated inside the outer ILR of the large-scale stellar bar/oval.

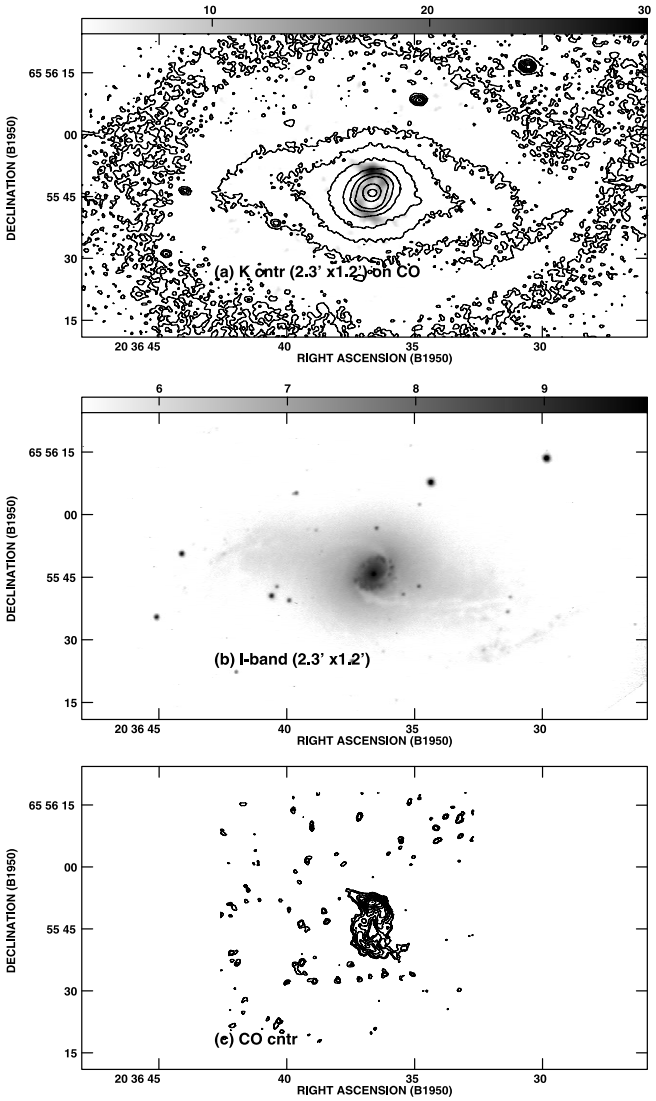

FIG. 10.—Relationship between the large-scale stellar bar, large-scale dust lanes, and circumnuclear CO morphology in NGC 6951. (*a*) The *K*-band image (*contours*) of NGC 6951 with a $2.'3 \times 1.'2$ (12.7 kpc × 6.9 kpc) field of view shows the inner region of the large-scale stellar bar, which has a semimajor axis of 28″ (5.2 kpc). The circumnuclear CO $J = 1 \rightarrow 0$ total intensity map (*gray scale*) is superposed, but note that its HPBW is only 65″ (6.1 kpc). (*b*) *I*-band image with the same field of view as the *K*-band image in (*a*). Two relatively straight dust lanes extend along the major axis of the large-scale stellar bar and are offset toward its leading edge. These dust lanes do not cross the center of the galaxy, but rather cross the bar minor axis and connect to a ring of SF of radius ~4″ (380 pc). (*c*) The CO $J = 1 \rightarrow 0$ total intensity map (*contours*) is displayed on the same scale as (*a*) and (*b*) to facilitate comparison. NGC 6951 has two spiral-shaped CO arms where the emission peaks at a radius $r \sim 6''$ (570 pc). The two CO peaks lie almost along the minor axis of the bar, and the CO arms connect to the two relatively straight dust lanes on the leading edge of the large-scale stellar bar. The CO and dust morphology are consistent with the piling up of gas near the OILR.

two dust lanes that are associated with the leading edges of a bar do not cross the center of the galaxy, but are offset along the bar minor axis, in the direction of x_2 orbits (e.g., Athanassoula 1992; Byrd et al 1994; Piner et al. 1995). The separation of the offset dust lanes provides a lower limit to $2R_{\rm OILR}$. Figures 10*a*–10*c* illustrate the case for the type II nonstarburst NGC 6951. The large-scale stellar bar of NGC 6951 has a semimajor axis of 28″ (5.2 kpc; Fig. 10*a*), and two relatively straight dust lanes are visible on its leading edge (Fig. 10*b*). As they approach the circumnuclear region, these dust lanes do not cross the center of the galaxy, but instead are offset along the bar minor axis. These dust lanes connect to the spiral-shaped CO arms where the two CO peaks lie almost along the minor axis of the stellar bar (Fig. 10*c*). The CO and dust morphology are consistent with the accumulation of gas near the OILR. Similar pairs of offset dust lanes are seen in the starbursts NGC 3504 and NGC 4102 and in the type II nonstarbursts NGC 3351 and NGC 4314.

A comparison of the lower limits on $R_{\rm OILR}$ (whether determined by method 1 or 2) with the azimuthally averaged molecular gas surface density $\Sigma_{\rm gas\text{-}m}$ (Fig. 7*a*) shows that the starbursts and type II nonstarbursts have their peak gas surface density and most of their circumnuclear gas inside or near the OILR of the stellar bar. Similar results are reported in studies of individual systems (e.g., Kenney et al. 1992; Knapen et al. 1995; Jogee

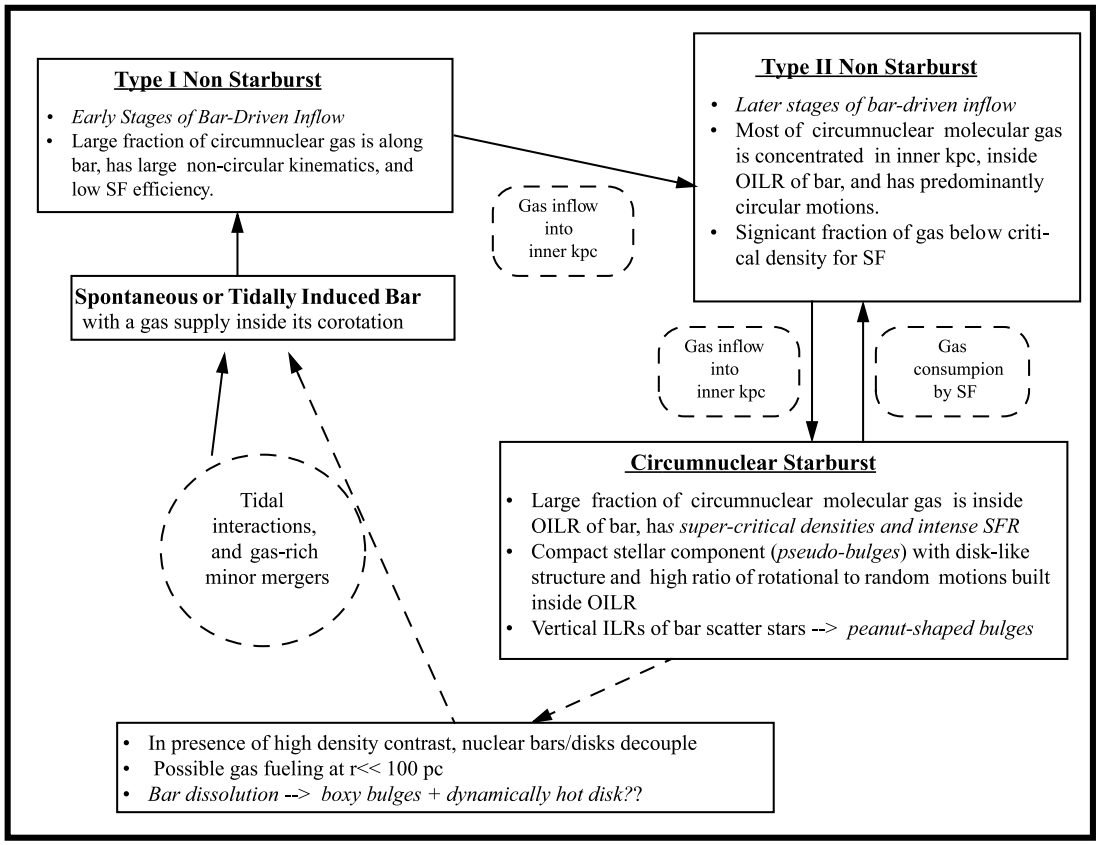

FIG. 11.—Bar-driven secular evolution. This figure sketches possible scenarios for bar-driven dynamical evolution and postulates potential evolutionary connections between the barred starbursts and nonstarbursts in our sample. We suggest that a strongly barred galaxy would show up as a type I nonstarburst in the early stages of bar-driven inflow, where large amounts of gas are still inflowing along the bar, have large noncircular motions, and are not forming stars efficiently. In the later stages where most of the circumnuclear gas has piled up inside the OILR of the bar, we may see a type II nonstarburst or even a circumnuclear starburst if most of the gas exceeds a critical density. The latter seems well represented by the Toomre value in our sample. Pseudobulges (Kormendy 1993) or compact stellar components with disklike properties can be built in the inner kiloparsec, as seen in our sample galaxy NGC 3351. Over its lifetime, a disk galaxy can undergo numerous episodes of bar-driven gas inflow and gradually build up its central mass concentration and bulge, provided an adequate gas supply is maintained inside the corotation radius of the bar. However, if the central mass concentration becomes large enough, bar dissolution may occur, leaving behind a dynamically hot disk. It is as yet unclear whether tidal interactions and gas-rich accretions can lead to viable recurrent bar formation in such a disk.

1999, 2001; Jogee et al. 2002a, 2002b). However, the CO data do not enable us to determine whether the gas has flown past the IILR since the CO resolution (100–200 pc) is comparable to the upper limits on $R_{\rm IILR}$. However, we note that the *HST* images of many sample galaxies (e.g., NGC 4102, NGC 3504, NGC 4536, NGC 4314, NGC 3351, NGC 6951) show that SF does not extend inside the central 100 pc radius or so; this may be due to the IILR blocking further gas inflow. It is interesting that NGC 2782, which hosts a nuclear stellar bar (§ 11; Jogee et al. 1999), is the only starburst where *HST* images show the SF peaking at the center.

11. BAR-DRIVEN SECULAR EVOLUTIONARY SCENARIOS

In this penultimate section, we discuss potential evolutionary connections between the barred starbursts and nonstarbursts in our sample and how they fit into scenarios of bar-driven dynamical evolution.

The evidence presented in § 10 (based on the dynamical frequencies and dust morphologies) suggests that the starbursts and type II nonstarbursts have piled up most of their circumnuclear gas inside or near the OILR of the large-scale stellar bar. In contrast, the type I nonstarburst, such as NGC 4569, has an extended gas distribution extending out to $r \sim 2$ kpc (§ 7), with a large fraction of the gas still inflowing along the bar and exhibiting large noncircular motions.

We suggest that a barred galaxy would show up as a type I nonstarburst in the early stages of bar-driven inflow where large amounts of gas are still along the bar, experiencing shocks, torques, and large noncircular motions. A schematic illustration is shown in Figure 11. Examples of such systems might be NGC 4569 (§ 8), NGC 7479 (§ 8; Laine et al. 1999), NGC 7723 (Chevalier & Furenlid 1978), NGC 1300, and NGC 5383 (Tubbs 1982). During this phase, SF is suppressed or highly inefficient due to large velocity gradients, shear, and tidal forces (Elmegreen 1979) in the gas along the bar. The low SFR/$M_{\rm H2}$ along a strong bar, as typified by the type I nonstarburst, is fundamental in enabling a bar to efficiently increases the central mass concentration in the inner kiloparsec of galaxies. It is only when the gas inflow rate along the bar exceeds the SFR over the same region that an efficient mass buildup happens. Available estimates of gas inflow rates along large-scale stellar bars range from 1 to 4 $M_\odot$ yr^{-1} (Quillen et al. 1995; Laine et al. 1999; Regan et al. 1997). If we assume a conservative net inflow rate of 1 $M_\odot$ yr^{-1} along the bar into the inner kiloparsec radius, then over 1 Gyr a bar can increase the dynamical mass in the inner kiloparsec by 1×10^9 $M_\odot$, or a few percent. For instance, in our sample galaxies the dynamical mass (§ 5) enclosed within $r = 1$ kpc ranges from 6 to 30×10^9 $M_\odot$ (Fig. 12), and would increase by 6%–30%. In practice, the mass buildup may be slower due to starburst-driven gas outflows, which can be ~1 to

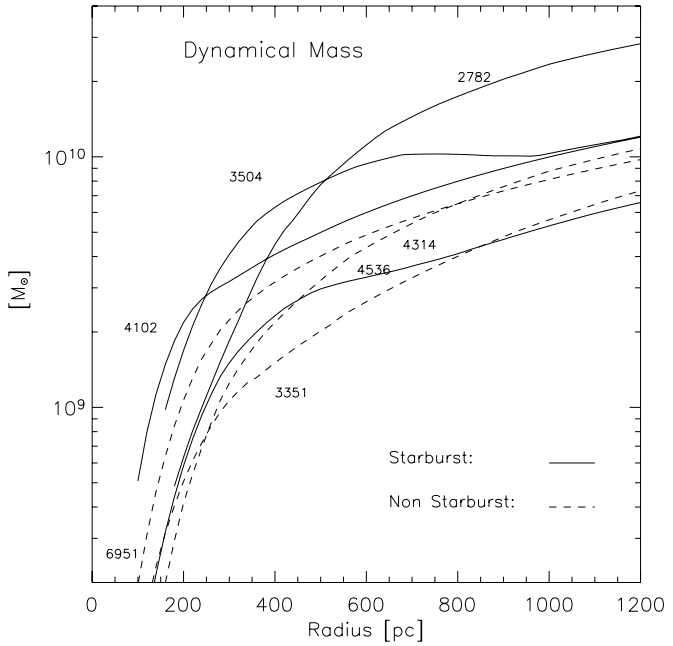

FIG. 12.—Enclosed dynamical mass within the inner kiloparsec. The dynamical mass ($M_{\rm dyn}$) enclosed within a given radius R is estimated from the rotation curve, assuming a spherically symmetric gas distribution. Values are shown only for sample barred galaxies for which a reliable rotation curve can be derived. For $R = 1$ kpc, $M_{\rm dyn}$ has a range of $(6-30) \times 10^9\ M_\odot$.

a few $M_\odot\ {\rm yr}^{-1}$ (e.g., Jogee et al. 1998 for the starburst NGC 2782; Heckman et al. 1990).

As discussed in §§ 8 and 10, after gas crosses the OILR it settles into a more axisymmetric distribution with predominantly circular motions. Thus, in the later stages of bar-driven inflow, a barred galaxy is expected to become a type II nonstarburst (Fig. 11). The instability analysis in § 8 suggests that gas concentrations that build up near the ILRs will undergo SF once the gas densities exceed the Safronov (1960)/Toomre (1964) critical density $\Sigma_{\rm crit} = (\alpha\kappa\sigma/\pi G)$. In the inner kiloparsec, the very high epicyclic frequency (several 100–1000 km s^{-1} kpc^{-1}) will naturally force $\Sigma_{\rm crit}$ to be high (e.g., several 100–1000 $M_\odot$ pc^{-2}), thereby enabling SF to occur only at high gas densities. Under this scenario, some type II nonstarbursts are prestarbursts that may eventually become starbursts (Fig. 11) if the gas density subsequently becomes supercritical.

The intense starbursts in our samples with circumnuclear SFRs of 3–11 $M_\odot\ {\rm yr}^{-1}$ will build compact young stellar disks or annuli inside the OILR. The interplay between the SFR, the outflow rate driven by starburst winds or jets, and the molecular gas supply will determine how massive such compact stellar components eventually will be. These compact stellar components, which form from cold gas within the inner kiloparsec, may belong to the class of so-called pseudobulges (Kormendy 1993), whose light distribution and kinematics are more consistent with a disk than with a spheroidal bulge component. Several studies have in fact reported that the central light distribution of many late-type galaxies are better represented by an exponential disklike component than an $r^{1/4}$ profile (e.g., de Jong 1996; Courteau et al. 1996).

As a typical starburst in our sample converts its molecular gas reservoir into such a compact disky stellar component, it is expected to transition into a type II nonstarburst, as the gas density in part of the wide gas annulus will soon become subcritical. One possible outcome is that SF shuts off first at lower radii (where $\Sigma_{\rm crit}$ is higher, the instability growth timescale $t_{\rm GI} \sim Q/\kappa$ is shorter and $\Sigma_{\rm SFR}$ is higher) such that we end up with a newly

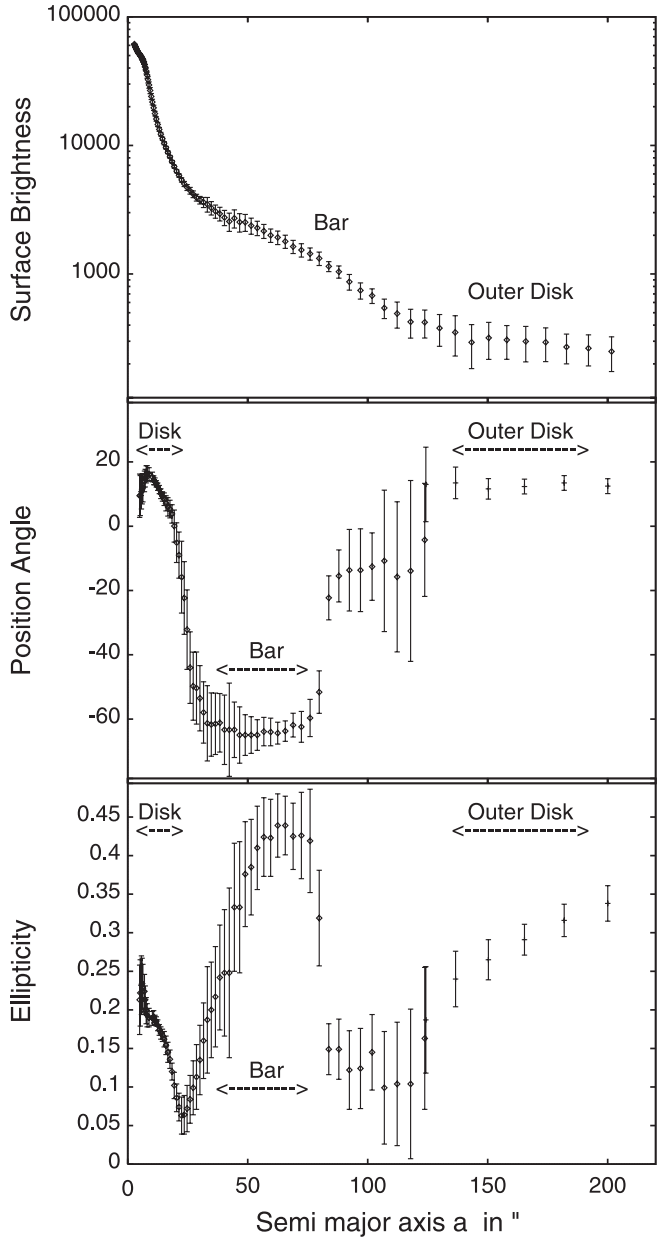

FIG. 13.—Evidence of a pseudobulge or compact disk in NGC 3351? The isophotal analysis of the K-band and R-band images of NGC 3351 is shown. Inside the inner kiloparsec radius, the ellipticity rises from a minimum value of 0.05 at $r \sim 1$ kpc to a maximum of $\sim$0.2 at a radius of 5″ (250 pc). The P.A. of the isophotes change from -60° in the region of the large-scale stellar bar to a value between 5° and 20° in the central 5″ (250 pc) radius. The central component has an ellipticity and P.A. that are similar to those of the outer disk, and a published high ratio of rotational to random motions.

built compact disky stellar component lying inside a thin star-forming gas ring. In our own sample, the type II nonstarburst NGC 3351 may provide a striking example of this process. Inside its thin CO ring, NGC 3351 hosts a central stellar component that has a high ratio of rotational to random motions (Kormendy 1983). Isophotal fits to the K- and R-band images of NGC 3351 (Fig. 13) show that this central component has an ellipticity and P.A. similar to those of the outer disk. Both the light distribution and kinematics would suggest that a compact stellar component with disklike properties has built up in the central $r = 6''$ (300 pc) of NGC 3351. Thus, in this framework some type II nonstarbursts may also be poststarbursts hosting a compact disky stellar component (Fig. 11). It should be noted that

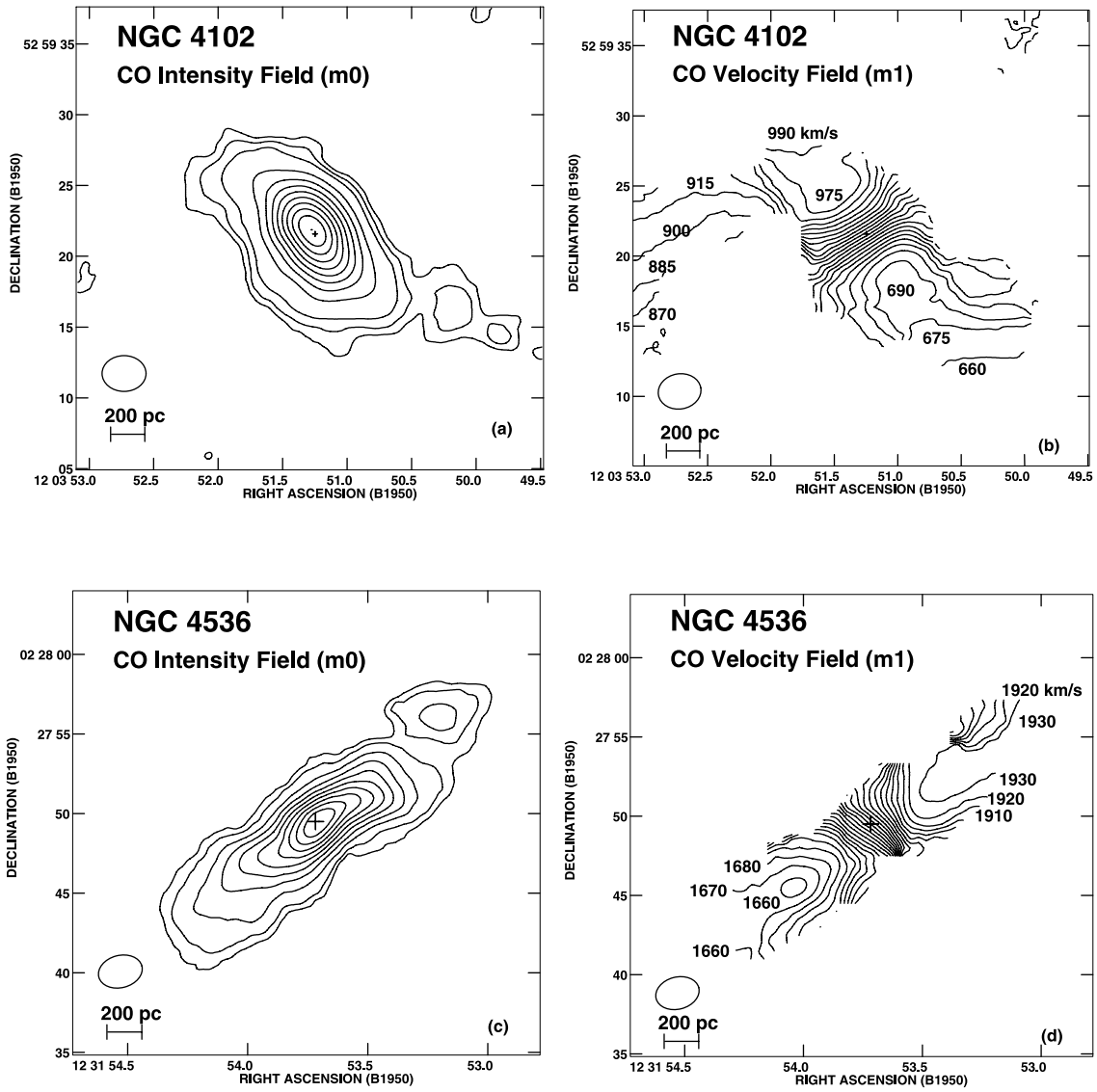

FIG. 14.—Molecular gas kinematics and distribution in individual starbursts. The CO intensity-weighted velocity (moment 1) fields and the CO total intensity (moment 0) maps of the starbursts (*a–b*) NGC 4102, (*c–d*) NGC 4536, (*e–f*) NGC 3504, (*g–h*) NGC 470, and (*i–j*) NGC 2782 are shown. The size of the synthesized beam is shown next to each map. The contour levels plotted are specified in Table 10. Relatively axisymmetric annuli or disks (NGC 4102, NGC 3504, NGC 4536) and elongated double-peaked morphologies (NGC 2782) are seen. The velocity field in the inner 500 pc radius is generally dominated by circular motions, with weaker noncircular components. In NGC 4102 and NGC 4536, there are faint gas streams that extend out, intersect the dust lanes on the leading edges of the large-scale stellar bar, and show noncircular motions. In NGC 2782, there are weak barlike streaming motions in the inner 400 pc radius, on the leading side of a nuclear stellar bar.

vertical instabilities (e.g., Sellwood 1993; Merritt & Sellwood 1994) and vertical ILRs associated with the bars (Combes et al. 1990) can scatter stars in the initially flat disky component to large scale heights, thereby enhancing or building a stellar bulge.

The overall schematic picture (Fig. 11) that emerges is that an episode of bar-driven gas inflow causes a barred galaxy to go through successive phases from a type I nonstarburst to a type II nonstarburst, which under the right conditions can undergo a starburst that will eventually evolve back into a type II nonstarburst. This picture would naturally explain why a one-to-one correlation is not seen between bars and powerful central starbursts, although in a statistical sense relatively luminous starbursts tend to be preferentially barred compared to normal galaxies (Hunt & Malkan 1999). Over its lifetime, a disk galaxy can undergo numerous episodes of bar-driven gas inflow characterized by these phases and gradually build up its central mass concentration and bulge, provided an adequate gas supply is maintained inside the corotation radius of the bar. This can be achieved by accreting gas-rich satellites in a barred disk galaxy or/and by externally inducing a new bar whose corotation radius encloses preexisting gas reservoirs at large radii. Minor (1:10) to moderate (1:4) mass ratio tidal interactions and mergers provide a natural way of doing both (Fig. 11) and are believed to be frequent over the last 8 Gyr since $z = 1$ (Jogee et al. 2003; Mobasher et al. 2004).

12. INDIVIDUAL GALAXIES

The molecular gas distribution and kinematics of individual starbursts and nonstarbursts are described below. Figures 14*a*–14*j* and 15*a*–15*f* show the total intensity (moment 0) and intensity-weighted velocity (moment 1) maps. For selected cases, *p-v* plots are shown if they can better the represent complex kinematics. The contour levels of the maps in all the figures are specified in Table 10.

12.1. *The Starbursts*

NGC 4102, NGC 4536, NGC 3504, and NGC 470.—Within the inner kiloparsec radius of the starbursts NGC 470, NGC

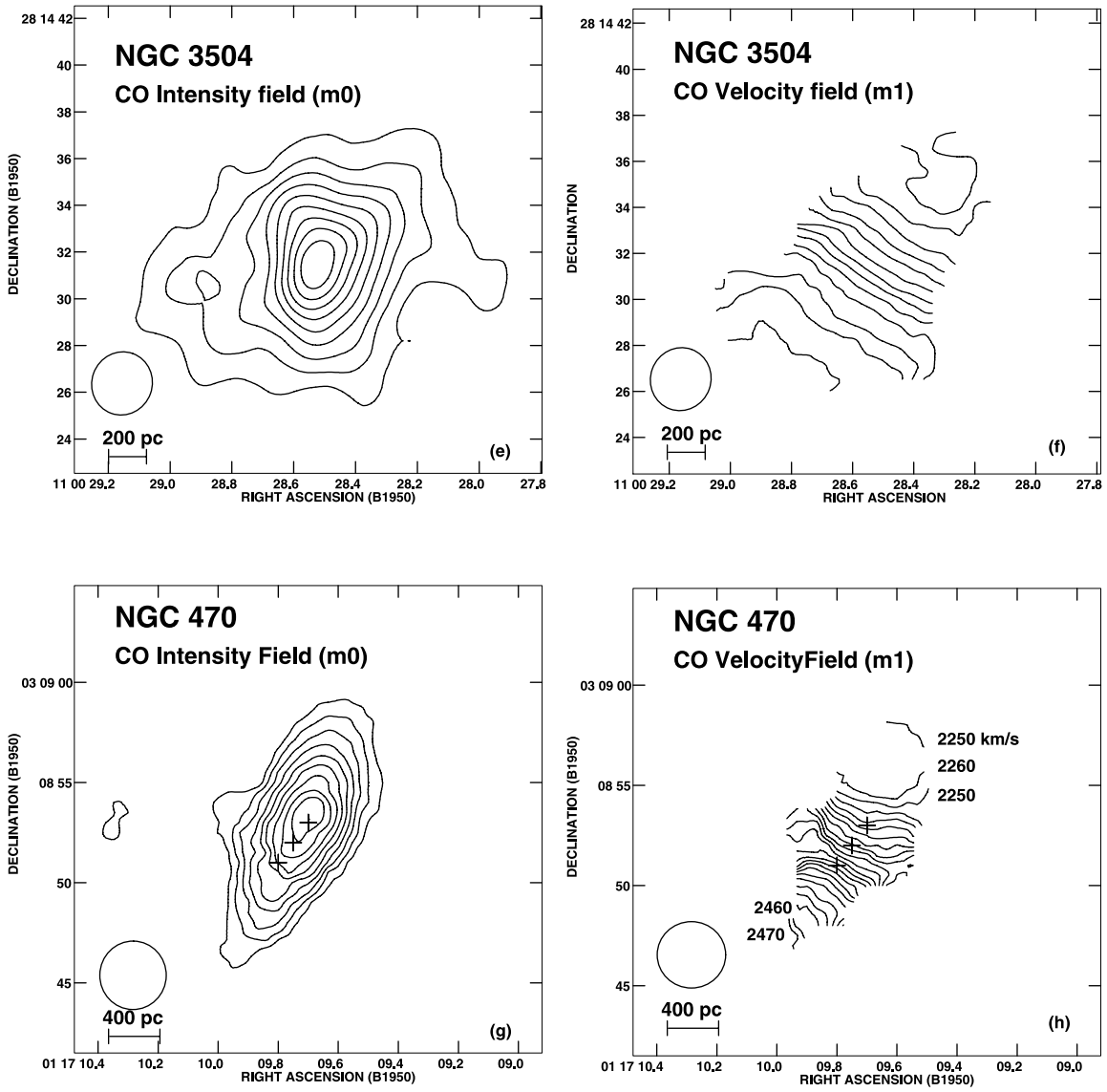

FIG. 14.—*Continued*

4102, NGC 3504, and NGC 4536, the molecular gas distribution (Figs. 14*a*–14*h*) observed in the sky plane looks relatively symmetric about the line of nodes and is elongated along that P.A. with an aspect ratio consistent with projection effects caused by the inclination of the galaxies. This implies that within the galactic plane of these four starbursts, most of the circumnuclear molecular gas has a relatively axisymmetric distribution of 300–600 pc radius. The moment 1 isovelocity contours (Figs. 14*a*–14*h*) in the inner 500 pc radius trace the characteristic spider diagram, suggesting the gas motions are predominantly circular. Several starbursts (NGC 4102, NGC 4536) show faint gas streams that extend from the relatively axisymmetric gas concentrations and curve along the leading edges of the large-scale stellar bar, connecting to the large-scale dust lanes. The gas streams show noncircular motions and are likely inflowing along the bar into the inner kiloparsec region.

NGC 2782.—The starburst galaxy NGC 2782 differs in several respects from the other starbursts. The CO morphology in the sky plane is nonaxisymmetric, double peaked, and barlike in the inner kiloparsec radius (Figs. 14*i* and 14*j*). Since the galaxy has a low inclination of $\sim 30^{\circ}$, this elongated morphology is not due to projection effects, but reflects the intrinsic gas distribution in the galactic plane. Jogee et al. (1999) have presented evidence that the CO properties are consistent with the molecular gas responding to a nuclear stellar bar of radius $\sim$1.3 kpc, identified via isophotal fits to NIR images. The CO barlike feature in NGC 2782 is offset in a leading sense with respect to the nuclear stellar bar and shows some noncircular kinematics (Jogee et al. 1999). The nuclear stellar bar appears to be fueling gas from the CO lobes located at a 1 kpc radius down into the central 200 pc radius, where a powerful central starburst is forming stars at a rate $\geq 3\ M_{\odot}\ \mathrm{yr}^{-1}$ (Jogee et al. 1998). It is striking that NGC 2782 is the only starburst in our sample where *HST* images show the SF peaking at the center. In contrast, the other starbursts do not show evidence of strong nuclear stellar bars, and their *HST* images show that SF does not extend into the inner 100 pc region.

12.2. *The Nonstarbursts*

NGC 6951.—There are two CO peaks at a radius of 6″ (550 pc) lying nearly perpendicular to the large-scale stellar bar whose P.A. is 85° (Fig. 3*b* or 10*a*). Fainter emission around the peaks forms two spiral-shaped streams that extend out and curve

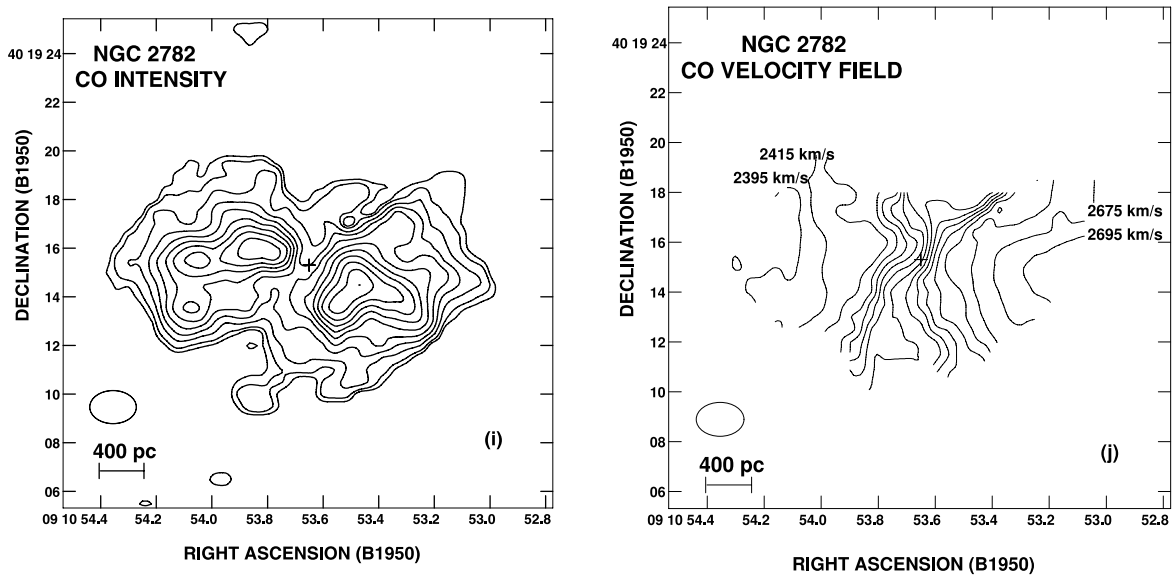

FIG. 14.—*Continued*

along the dust lanes on the leading edge of the large-scale bar. The molecular gas at the CO peaks and in the spiral streams shows complex noncircular motions (Figs. 15*a* and 15*b*). In NGC 6951, NGC 3351, and NGC 4314, the CO peaks lie near the OILR of the large-scale stellar bar (§ 10).

NGC 3351.—The CO emission shows two peaks at a radius of $\sim 7''$ (350 pc). As in NGC 6951, the two CO peaks lie nearly perpendicular to the large-scale stellar bar, whose P.A. is 110° (Fig. 3*b*). The CO emission around the peaks appears to connect to the dust lanes, which lie on the leading edge of the bar. The isovelocity contours curve near the CO peaks, suggesting noncircular streaming motions (Figs. 15*c* and 15*d*). Interior to the CO peaks, the *p-v* plot along the kinematic minor axis, where we are sensitive to the radial in-plane motion and vertical out-of-plane motion, shows complex noncircular kinematics.

NGC 4314.—Most of the gas is concentrated in a multiple-peaked relatively circular ring of radius $5''$–$7''$ (240–400 pc). Two faint CO spurs extend from the ring and intersect the dust lanes that lie on the leading edge of the large-scale stellar, whose P.A. is 143° (Fig. 3*b*). Noncircular motions of 10–65 km s^{-1} are detected in the CO spurs (Figs. 15*e* and 15*f*). The CO peaks lie near the OILR of the large-scale stellar bar (§ 10). Furthermore, inside the clumpy CO ring, ground-based (Friedli et al. 1996) and *HST* images of NGC 4314 reveal a nuclear stellar bar of radius $4''$ (200 pc) at a P.A. of $-3°$ to $-12°$. In contrast to NGC 2782, the CO emission in NGC 4314 is not primarily concentrated along the nuclear stellar bar, but instead forms a clumpy ring at the end of the nuclear bar. The reason for such different gas and SF distributions in the two nuclear bars may be evolutionary in nature. In the case of NGC 4314, we may be seeing gas

TABLE 10
CONTOUR LEVELS PLOTTED IN FIGURES

NGC Number	Figure	Contour Levels
	Circumnuclear Starbursts	
470	Figs. 3, 5, 14	2.48 Jy beam^{-1} km s^{-1} × (1, 2, 3, 4, 5, 6, 7, 8, 9, 10)
	Fig. 14	(2200, 2210, 2220, . . . , 2470, 2480, 2490) km s^{-1}
2782	Figs. 3, 5, 14	7.15 Jy beam^{-1} km s^{-1} × (1, 2, 3, 4, 5, 6, 7, 8, 9, 10)
	Fig. 14	(2275, 2295, 2315, . . . , 2815, 2835, 2855) km s^{-1}
3504	Figs. 3, 5, 14	8.33 Jy beam^{-1} km s^{-1} × (0.5, 1, 2, 3, 4, 5, 6, 7, 8, 9, 10)
	Fig. 14	(585, 600, 615, . . . , 990, 1005, 1020) km s^{-1}
4102	Figs. 3, 5, 14	8.33 Jy beam^{-1} km s^{-1} × (0.5, 1, 2, 3, 4, 5, 6, 7, 8, 9, 10)
	Fig. 14	(585, 600, 615, . . . , 990, 1005, 1020) km s^{-1}
4536	Figs. 3, 5, 14	3.05 Jy beam^{-1} km s^{-1} × (1, 2, 3, 4, 5, 6, 7, 8, 9, 10)
	Fig. 14	(1640, 1650, 1660, . . . , 1910, 1920, 1930) km s^{-1}
	Circumnuclear Nonstarbursts	
3351	Figs. 3, 5, 15	1.84 Jy beam^{-1} km s^{-1} × (1, 2, 3, 4, 5, 6, 7, 8, 9, 10)
	Fig. 15	(660, 670, 680, . . . , 930, 940, 950) km s^{-1}
4314	Figs. 3, 5, 15	1.34 Jy beam^{-1} km s^{-1} × (1, 2, 3, 4, 5, 6, 7, 8, 9, 10)
	Fig. 15	(915, 930, 945, . . . , 1050, 1065, 1080) km s^{-1}
4569	Figs. 3, 5, 15	3.20 Jy beam^{-1} km s^{-1} × (1, 2, 3, 4, 5, 6, 7, 8, 9, 10)
6951	Figs. 3, 5, 15	2.92 Jy beam^{-1} km s^{-1} × (1, 2, 3, 4, 5, 6, 7, 8, 9, 10)
	Fig. 15	(1275, 1290, 1305, . . . , 1680, 1695, 1710) km s^{-1}

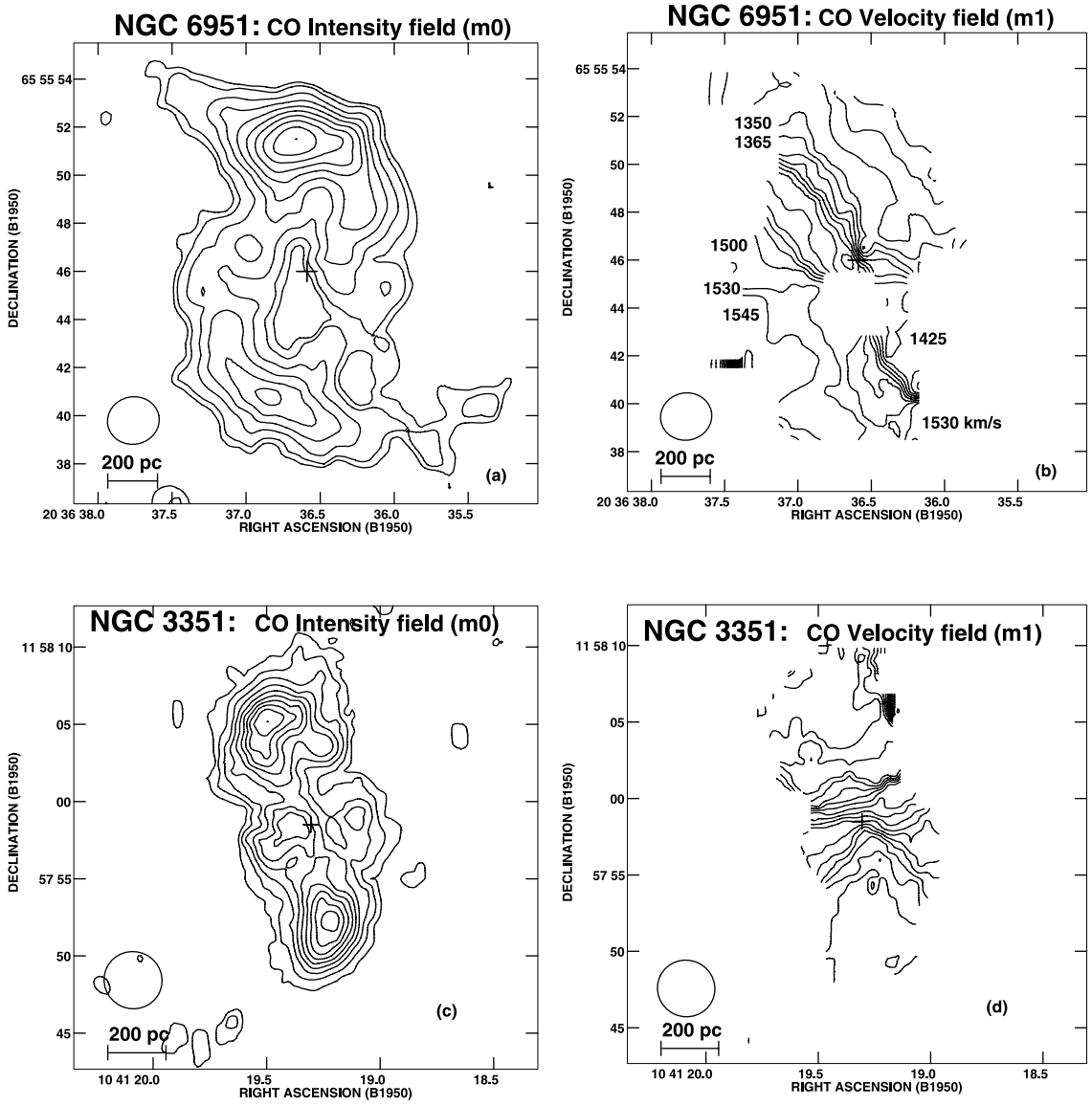

FIG. 15.—Molecular gas kinematics and distribution in the individual nonstarbursts. As in Fig. 14, but for nonstarbursts (*a*–*b*) NGC 6951, (*c*–*d*) NGC 3351, and (*e*–*f*) NGC 4314. The contour levels plotted are specified in Table 10. NGC 6951 has two spiral-shaped CO arms where the CO emission peaks at a radius $r \sim 6''$ (570 pc). NGC 3351 hosts two CO peaks at a radius $r \sim 7''$ (350 pc). In NGC 4314, there is a relatively circular CO ring of $8''$ (400 pc) radius from which extend two CO spurs/streams. The CO peaks in both NGC 6951 and NGC 3351 lie almost along the minor axis of the large-scale stellar bar. The CO arms in NGC 6951, the fainter emission around the CO peaks in NGC 3351, and the two CO spurs in NGC 4314 intersect the dust lanes on the leading edge of the large-scale stellar bar and show noncircular motions.

that is outside the corotation of a nuclear bar that formed earlier (Friedli & Martinet 1993). Conversely, in NGC 2782 we may be witnessing the early decoupling phase of a nuclear stellar bar induced by gas inside the OILR of the large-scale bar.

NGC 4569.—This galaxy (Figs. 6*a*–6*d*) differs from the above three nonstarbursts in that it has a highly extended molecular gas distribution with complex kinematics and large line widths of $\sim$150 km s^{-1}. A large fraction of the gas lies outside the inner kiloparsec radius and extends out to a radius of $20''$ (1.7 kpc), at a P.A. similar to that of the large-scale stellar bar (Figs. 6*a* and 6*b*). This gas has highly noncircular kinematics, as shown in the *p*-*v* plots along the kinematic major and minor axes (Figs. 6*c* and 6*d*). Along the kinematic major axis, velocities are generally positive (i.e., above the systemic value of -235 km s^{-1}) on the northeastern side, and negative on the southwest side. However, at a radius of $5''$ (400 pc), near the feature marked "N1" in Figure 6*c*, the velocities change from +100 km s^{-1} to a forbidden velocity of -75 km s^{-1}. This indicates the presence of noncircular motions caused by in-plane azimuthal streaming motions or/and vertical motions out of the plane. As discussed in § 3, the CO properties of NGC 4569 are consistent with the early phases of bar-driven/tidally driven gas inflow.

NGC 3359.—The interferometric observations captured less than 30% of the single-dish flux, in contrast to the other sample galaxies (Table 5). The moment 0 map of NGC 3359 in Figure 3*b* shows a very patchy CO distribution made up of a few clumps that lie away from the center. The present observations indicate that there is no bright centrally peaked CO distribution in the inner 500 pc of NGC 3359. The missing single-dish flux may come from extended gas and/or diffuse low surface brightness CO in the central regions. As discussed in § 3, several authors have proposed that the large-scale stellar bar in NGC 3359 is young and may have been tidally triggered, and it is possible that there are significant amounts of gas farther out along the bar. To resolve this issue,

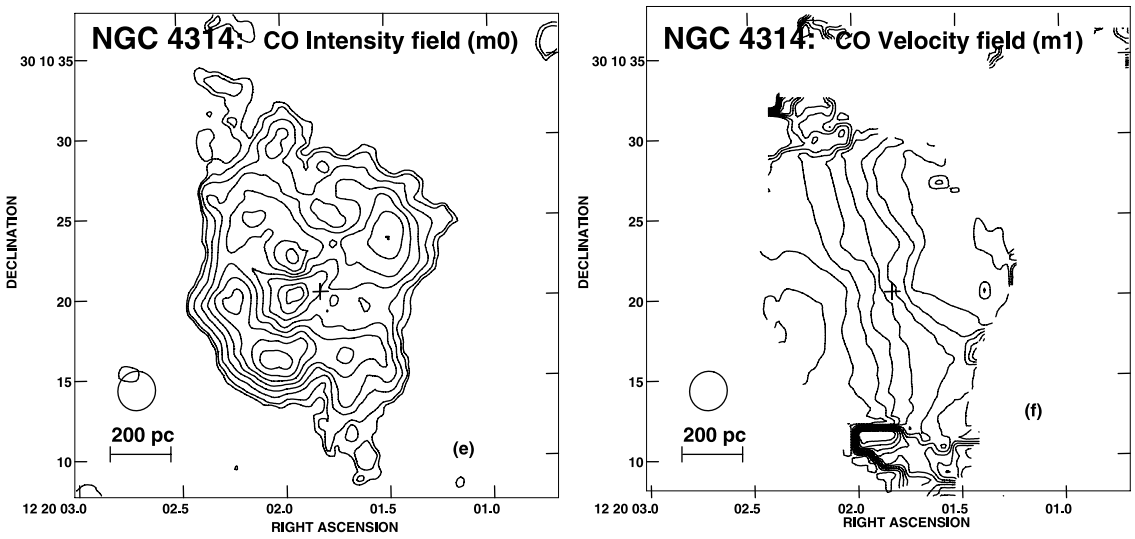

FIG. 15.—*Continued*

future interferometric observations of a larger field of view using a more compact array configuration needs to be carried out.

13. SUMMARY AND CONCLUSIONS

There is compelling observational and theoretical evidence that bars efficiently redistribute angular momentum in galaxies and drive gas inflows into the circumnuclear (inner 1–2 kpc) region. However, only a few high-resolution studies based on a large sample of galaxies have been carried out on the fate of gas in this region. In this study, we characterize the molecular environment, the onset of starbursts, and the secular evolution in the circumnuclear region of barred galaxies. We use a sample of local ($D < 40$ Mpc) barred nonstarbursts and starbursts having high-resolution ($\sim$200 pc) CO $J = 1 \rightarrow 0$, optical, NIR, Hα, RC, Brγ, and archival *HST* observations. Our results are summarized as follows.

1. The circumnuclear regions of barred galaxies host 3×10^8 to 2×10^9 $M_\odot$ of molecular gas and have developed a molecular environment that differs markedly from that in the outer disk of galaxies. It includes molecular gas surface densities of 500–3500 $M_\odot$ pc^{-2}, gas mass fractions of 10%–30%, epicyclic frequencies of several 100 to several 1000 km s^{-1} kpc^{-1}, and velocity dispersions of 10–40 km s^{-1}. In this environment, gravitational instabilities set in only at very high gas densities (a few 100–1000 $M_\odot$ pc^{-2}), but once triggered, they grow rapidly on a timescale of a few Myr. This high-density, short-timescale "burst" mode may explain why the most intense starbursts tend to be in the central parts of galaxies. Furthermore, the high-pressure, high-turbulence ISM can lead to the formation of clouds with high internal dispersion and mass and hence may favor the formation of massive clusters, as suggested by Elmegreen et al. (1993). The molecular environment in the inner kiloparsec of the ULIRG galaxy Arp 220 is a scaled-up version of the one in these barred galaxies, suggesting that interactions build up even more extreme conditions.

2. We suggest that the wide variety in CO morphologies is due to different stages of bar-driven inflow. A nonstarburst such as NGC 4569, which is in the early stages of bar-driven inflow, has a highly extended molecular gas distribution where a large fraction of the circumnuclear gas is still along the large-scale stellar bar, outside the outer inner Lindblad resonance (OILR). This gas shows large noncircular kinematics and is not forming stars efficiently. Several other galaxies studied by others, such as NGC 7479 (Laine et al. 1999), NGC 7723 (Chevalier & Furenlid 1978), NGC 1300, and NGC 5383 (Tubbs 1982), may be in a similar phase. In contrast, we present dynamical and morphological evidence that the other nonstarbursts and starbursts are in later stages of bar-driven inflow. Most of their circumnuclear gas is inside or near the OILR of the bar and has predominantly circular motions. Across the sample, we estimate upper limits in the range 43–115 km s^{-1} kpc^{-1} for the bar pattern speed and an OILR radius of >500 pc.

3. The barred starbursts and nonstarbursts have circumnuclear SFRs of 3–11 and 0.1–2 $M_\odot$ yr^{-1}, respectively. For a given amount of molecular hydrogen ($M_{\rm H2}$) in the inner 1–2 kpc (assuming a standard CO-to-H_2 conversion factor), barred galaxies can show an order of magnitude variation in the SFR/$M_{\rm H2}$ over this region. This range seems related to the fact that the gas surface densities in the starbursts are larger (1000–3500 $M_\odot$ pc^{-2}) and close to the Toomre critical density over a large region. The Toomre Q parameter reaches its minimum value of $\sim$1–2 in the region of SF, despite an order of magnitude variation in the gas surface density and epicyclic frequency. This suggests that the onset of gravitational instabilities, as characterized by Q, plays an important role even in the inner kiloparsec region.

4. The dynamical mass enclosed within the inner kiloparsec radius of the barred galaxies in our sample is $(6–30) \times 10^9$ $M_\odot$. Molecular gas makes up 10%–30% of the dynamical mass, and in the circumnuclear starbursts, it is fueling an SFR of 3–11 $M_\odot$ yr^{-1} in the inner kiloparsec. As these starbursts use up their gas and evolve into the poststarburst phase, they will build young, massive, high-V/σ stellar components within the inner kiloparsec, inside the OILR of the large-scale bar. Such compact stellar components will likely belong to the class of pseudobulges (Kormendy 1993), whose light distribution and kinematics are more consistent with a disk than with a spheroidal bulge component. We present evidence of such a component in NGC 3351, which seems to be in a postburst phase. The observations are consistent with the idea that over a galaxy's lifetime, it can experience numerous episodes of bar-driven/tidally driven gas inflows, which lead to a gradual buildup of its central mass concentration,

the formation of pseudobulges, and perhaps even secular evolution along the Hubble sequence.

Support for this work was generously provided by NSF grant AST 99-81546 and a grant from the K. T. and E. L. Norris Foundation. S. J. also acknowledges support from the National Aeronautics and Space Administration under LTSA grant NAG5-13063 issued through the Office of Space Science, a Grant-in-Aid of Research from Sigma Xi (The Scientific Research Society), an AAUWEF Fellowship, and a Zonta International Amelia Earhart Fellowship.

REFERENCES

Aalto, S., et al. 1994, A&A, 286, 365
———. 1995, A&A, 300, 369
Athanassoula, E. 1992, MNRAS, 259, 345
———. 2002, ApJ, 569, L83
Baker, A. J. 2000, Ph.D. thesis, Caltech
Ball, R. 1986, ApJ, 307, 453
Benedict, G. F., Smith, B. J., & Kenney, J. D. P. 1996, AJ, 111, 1861
Berentzen, I., Shlosman, I., & Jogee, S. 2005, ApJ, submitted (astro-ph/0501352)
Binggeli, B., Sandage, A., & Tammann, G. A. 1985, AJ, 90, 1681
Binney, J., & Tremaine, S. 1987, Galactic Dynamics (Princeton: Princeton Univ. Press)
Bloemen, J. B. G. M., et al. 1986, A&A, 154, 25
Byrd, G., et al. 1994, AJ, 108, 476
Cayatte, V., Kotanyi, C., Balkowski, C., & van Gorkom, J. H. 1994, AJ, 107, 1003
Chevalier, R. A., & Furenlid, I. 1978, ApJ, 225, 67
Combes, F., Debasch, F., Friedli, D., & Pfenniger, D. 1990, A&A, 233, 82
Combes, F., & Gerin, M. 1985, A&A, 150, 327
Condon, J. J. 1987, ApJS, 65, 485
———. 1992, ARA&A, 30, 575
Condon, J. J., Anderson, E., & Broderick, J. J. 1995, AJ, 109, 2318
Condon, J. J., Condon, M. A., Gisler, G., & Puschell, J. J. 1982, ApJ, 252, 102
Condon, J. J., Helou, G., Sanders, D. B., & Soifer, T. B. 1990, ApJS, 73, 359
Condon, J. J., & Yin, Q. F. 1990, ApJ, 357, 97
Contopoulos, G., & Papayannopoulos, T. 1980, A&A, 92, 33
Courteau, S., de Jong, R. S., & Broeils, A. H. 1996, ApJ, 457, L73
Das, M., & Jog, C. J. 1995, ApJ, 451, 167
Debattista, V. P., & Sellwood, J. A. 2000, ApJ, 543, 704
Deharveng, J. M., et al. 1994, A&A, 289, 715
de Jong, R. S. 1996, A&A, 313, 45
de Vaucouleurs, G., de Vaucouleurs, A., Corwin, Jr., H. G., Buta, R. J., Paturel, G., & Fouqué, P. 1991, Third Reference Catalogue of Bright Galaxies (New York: Springer) (RC3)
Devereux, N. A. 1989, ApJ, 346, 126
Dickey, J. M., Hanson, M. M., & Helou, G. 1990, ApJ, 352, 522
Dickman, R. L. 1975, ApJ, 202, 50
Dickman, R. L., Snell, R. L., & Schloerb, F. P. 1986, ApJ, 309, 326
Eder, J. A. 1990, Ph.D. thesis, Yale Univ.
Elmegreen, B. G. 1979, ApJ, 231, 372
———. 1989, ApJ, 338, 178
———. 1990, ApJ, 357, 125
———. 1995, MNRAS, 275, 944
Elmegreen, B. G., Elmegreen, D. M., & Hirst, A. C. 2004, ApJ, 612, 191
Elmegreen, B. G., Kaufman, M., & Thomasson, M. 1993, ApJ, 412, 90
Elmegreen, D. M., Chromey, F. R., Santos, M., & Marshall, D. 1997, AJ, 114, 1850
Eskridge, P. B., et al. 2002, ApJS, 143, 73
Friedli, D., & Benz, W. 1995, A&A, 301, 649
Friedli, D., Benz, W., & Kennicutt, R., Jr. 1994, ApJ, 430, L105
Friedli, D., & Martinet, L. 1993, A&A, 277, 27
Friedli, D., et al. 1996, A&AS, 118, 461
Gammie, C. F., Ostriker, J. P., & Jog, C. J. 1991, ApJ, 378, 565
Geller, M. J., & Huchra, J. P. 1983, ApJS, 52, 61
Giovanelli, R., & Haynes, M. P. 1983, AJ, 88, 881
Giuricin, G., Tamburni, L., Mardirossin, F., Mezzetti, M., & Monaco, P. 1994, ApJ, 427, 202
Goldreich, P., & Lynden-Bell, D. 1965, MNRAS, 130, 125
Grosbøl, P. J. 1985, A&AS, 60, 261
Handa, T., Sofue, Y., & Nakai, N. 1991, in IAU Symp. 146, Dynamics of Galaxies and Their Molecular Cloud Distributions, ed. F. Combes & F. Casoli (Dordrecht: Kluwer), 156
Heckman, T. M., Armus, L., & Miley, G. K. 1990, ApJS, 74, 833
Helfer, T. T., & Blitz, L. 1993, ApJ, 419, 86
Helfer, T. T., et al. 2001, Ap&SS, 276, 1131
Heller, C. H., & Shlosman, I. 1996, ApJ, 471, 143
Hunt, L. K., & Malkan, M. A. 1999, ApJ, 516, 660
Jog, C. J., & Solomon, P. M. 1984, ApJ, 276, 127
Jogee, S. 1999, Ph.D. thesis, Yale Univ.
———. 2001, in Starburst Galaxies: Near and Far, ed. L. Tacconi & D. Lutz (Heidelberg: Springer), 182
———. 2005, in AGN Physics on All Scales, ed. D. Alloin, R. Johnson, & P. Lira (Berlin: Springer), in press (astro-ph/0408383)
Jogee, S., & Kenney, J. D. P. 1996, in IAU Colloq. 157, Barred Galaxies, ed. R. Buta, D. A. Crocker, & B. G. Elmegreen (ASP Conf. Ser. 91; San Francisco: ASP), 230
Jogee, S., Kenney, J. D. P., & Smith, B. J. 1998, ApJ, 494, L185
———. 1999, ApJ, 526, 665
Jogee, S., Knapen, J. H., Laine, S., Shlosman, I., Scoville, N. Z., & Englmaier, P. 2002a, ApJ, 570, L55
Jogee, S., Shlosman, I., Laine, S., Englmaier, P., Knapen, J. H., Scoville, N. Z., & Wilson, C. D. 2002b, ApJ, 575, 156
Jogee, S., et al. 2003, in IAU Symp. 216, Maps of the Cosmos, meeting abstracts
———. 2004a, ApJ, 615, L105
———. 2004b, in Penetrating Bars through Masks of Cosmic Dust: The Hubble Tuning Fork Strikes a New Note, ed. D. L. Block, I. Puerari, K. C. Freeman, R. Groess, & E. K. Block (Dordrecht: Springer), 291
Kenney, J. D. P., Carlstrom, J. E., & Young, J. S. 1993, ApJ, 418, 687
Kenney, J. D. P., & Lord, S. D. 1991, ApJ, 381, 118
Kenney, J. D. P., Wilson, C. D., Scoville, N. Z., Devereux, N. A., & Young, J. S. 1992, ApJ, 395, L79
Kenney, J. D. P., & Young, J. S. 1989, ApJ, 344, 171
Kennicutt, R. C., Jr. 1983, ApJ, 272, 54
———. 1989, ApJ, 344, 685
———. 1998a, ARA&A, 36, 189
———. 1998b, ApJ, 498, 541
Kim, W., Ostriker, E. C., & Stone, J. M. 2002, ApJ, 581, 1080
Knapen, J. H., Shlosman, I., & Peletier, R. F. 2000, ApJ, 529, 93
Knapen, J. H., et al. 1995, ApJ, 454, 623
Kohno, K., Kawabe, R., & Vila-Vilaró, B. 1999, ApJ, 511, 157
Kormendy, J. 1983, ApJ, 265, 632
———. 1993, in IAU Symp. 153, Galactic Bulges, ed. H. DeJonghe & H. J. Habing (Dordrecht: Kluwer), 209
Kormendy, J., & Kennicutt, R. C. 2004, ARA&A, 42, 603
Kwan, J. 1979, ApJ, 229, 567
Laine, S., & Heller, C. H. 1999, MNRAS, 308, 557
Laine, S., Kenney, J. D. P., Yun, M. S., & Gottesman, S. T. 1999, ApJ, 511, 709
Larson, R. B. 1985, MNRAS, 214, 379
———. 1998, MNRAS, 301, 569
Maiolino, R., Ruiz, M., Rieke, G. H., & Papdopoulos, P. 1997, ApJ, 485, 552
Martin, P. 1995, AJ, 109, 2428
Martin, P., & Roy, R. 1995, ApJ, 445, 161
Merritt, D., & Sellwood, J. A. 1994, ApJ, 425, 551
Mobasher, M., Jogee, S., Dahlen, T., de Mello, D., Lucas, R. A., Conselice, C. J., Grogin, N. A., & Livio, M. 2004, ApJ, 600, L143
Muñoz-Tuñon, C., Vilchez, J. M., Castaneda, H. O., & Beckman, J. E. 1989, Ap&SS, 157, 165
Padin, S., Scott, S. L., Woody, D. P., Scoville, N. Z., Seling, T. V., Finch, R. P., Giovanine, C. J., & Lawrence, R. P. 1991, PASP, 103, 461
Pfenniger, D., & Norman, C. 1990, ApJ, 363, 391
Piner, B., Glenn, S., James, M., & Teuben, P. J. 1995, ApJ, 449, 508
Pompea, S. M., & Rieke, G. H. 1990, ApJ, 356, 416
Puxley, P. J., Hawarden, T. G., & Mountain, C. M. 1988, MNRAS, 234, 29P
———. 1990, ApJ, 364, 77
Quillen, A. C., Frogel, J. A., Kenney, J. D. P., Pogge, R. W., & DePoy, D. L. 1995, ApJ, 441, 549
Regan, M. W., Thornley, M. D., Helfer, T. T., Sheth, K., Wong, T., Vogel, S. N., Blitz, L., & Bock, D. C.-J. 2001, ApJ, 561, 218
Regan, M. W., Vogel, S. N., & Teuben, P. J. 1997, ApJ, 482, L143
Safronov, V. S. 1960, Ann. d'Astrophys., 23, 979
Sage, L. J. 1993, A&AS, 100, 537
Saha, A., Sandage, A., Labhardt, L., Tammann, G. A., Macchetto, F. D., & Panagia, N. 1996, ApJ, 466, 55
Saikia, D. J., Pedlar, A., Unger, S. W., & Axon, D. J. 1994, MNRAS, 270, 46

Sakamoto, K., Scoville, N. Z., Yun, M. S., Crosas, M., Genzel, R., & Tacconi, L. J. 1999, ApJ, 514, 68
Sandage, A., & Bedke, J. 1994, The Carnegie Atlas of Galaxies (Washington, DC: Carnegie Institution)
Schweizer, F., & Seitzer, P. 1988, ApJ, 328, 88
Scoville, N. Z., & Sanders, D. B. 1987, in Interstellar Processes, ed. D. J. Hollenbach & H. A. Thronson (Dordrecht: Reidel), 21
Scoville, N. Z., Sanders, D. B., & Clemens, D. P. 1986, ApJ, 310, L77
Scoville, N. Z., Yun, M. S., & Bryant, P. M. 1997, ApJ, 484, 702
Scoville, N. Z., et al. 1987, ApJS, 63, 821
———. 1993, PASP, 105, 1482
Sellwood, J. A. 1993, in IAU Symp. 153, Galactic Bulges, ed. H. DeJonghe & H. J. Habing (Dordrecht: Kluwer), 391
Shaw, M., Axon, D., Probst, R., & Gatley, I. 1995, MNRAS, 274, 369
Sheth, K., Vogel, S. N., Regan, M. W., Thornley, M. D., & Teuben, P. J. 2005, ApJ, in press (astro-ph/0505393)
Shlosman, I., Frank, J., & Begelman, M. C. 1989, Nature, 338, 45
Smith, B. J. 1994, AJ, 107, 1695
Soifer, B. T., Boehmer, L., Neugebauer, G., & Sanders, D. B. 1989, AJ, 98, 766
Solomon, P. M., Rivolo, A. R., Barrett, J., & Yahil, A. 1987, ApJ, 319, 730
Strong, A. W., et al. 1988, A&A, 207, 1
Tacconi, L. J., & Young, J. S. 1986, ApJ, 308, 600
Taylor, C. L., et al. 1994, AJ, 107, 971
Toomre, A. 1964, ApJ, 139, 1217
Tubbs, A. D. 1982, ApJ, 255, 458
Tully, R. B. 1988, Nearby Galaxies Catalog (Cambridge: Cambridge Univ. Press)
van den Bergh, S. 1976, ApJ, 206, 883
Vila, M. B., Pedlar, A., Davies, R. D., Hummel, E., & Axon, D. J. 1990, MNRAS, 242, 379
Vila-Costas, M. B., & Edmunds, M. G. 1992, MNRAS, 259, 121
Wall, W. F., & Jaffe, D. T. 1990, ApJ, 361, L45
Wozniak, H., Friedli, D., Martinet, L., Martin, P., & Bratschi, P. 1995, A&AS, 111, 115
Young, J. S., & Scoville, N. Z. 1991, ARA&A, 29, 581
Young, J. S., et al. 1995, ApJS, 98, 219